infrastructures

MDPI

Article

Ternary Gypsum–Cement–Pozzolanic Compositions for 3D Printing: Mix Design, Rheology and Long-Term Performance

Genadijs Sahmenko, Girts Bumanis, Maris Sinka, Peteris Slosbergs, Alise Sapata, Diana Bajare * and Vjaceslavs Lapkovskis *

Institute of Sustainable Building Materials and Engineering Systems, Faculty of Civil and Mechanical Engineering, Riga Technical University, Kipsalas 6A, LV-1048 Riga, Latvia; genadijs.sahmenko@rtu.lv (G.S.); girts.bumanis@rtu.lv (G.B.); maris.sinka@rtu.lv (M.S.); peteris.slosbergs@edu.rtu.lv (P.S.); alise.sapata@rtu.lv (A.S.)

* Correspondence: diana.bajare@rtu.lv (D.B.); vjaceslavs.lapkovskis@rtu.lv (V.L.)

Abstract

Ternary gypsum–cement–pozzolan (GCP) binders represent a promising low-carbon alternative to traditional Portland cement-based systems for additive 3D printing (3DP). This study presents a systematic three-stage experimental framework for the development of printable and durable GCP mixtures: (i) optimisation of gypsum–cement–metakaolin binder proportions based on a ternary diagram for 25 formulations, (ii) comparative evaluation of different pozzolanic additives and secondary gypsum sources alongside comprehensive durability testing, and (iii) adaptation of the optimised mixtures for 3DP, focusing on rheological properties. The optimal composition was determined with 55 wt% gypsum, 22.5 wt% Portland cement, and 22.5 wt% metakaolin, achieving a 28-day wet compressive strength of 36.2 MPa and a softening coefficient of 0.85. Successful integration of secondary gypsum sources was demonstrated. The GCP 3DP mixtures were developed with water/binder ratios of 0.38–0.45 and sand/binder ratios of 0.5–1.4, with an open time of 20–40 min. The mixtures exhibit pronounced thixotropic behaviour, characterised by increasing yield stress over time and relatively stable plastic viscosity. Printability tests confirmed the stable application of 29–39 layers before structural buckling. 3DP under laboratory conditions successfully demonstrated the feasibility of producing architectural and structural elements from sustainable GCP compositions.

Keywords: 3D printing; GCP compositions; rheology; durability; printability; buildability; secondary gypsum; metakaolin; mechanical properties; sustainable materials

Check for updates

Academic Editors: Dayou Luo and Kejin Wang

Received: 9 March 2026
Revised: 17 April 2026
Accepted: 20 April 2026
Published: 28 April 2026

Copyright: © 2026 by the authors. Licensee MDPI, Basel, Switzerland. This article is an open access article distributed under the terms and conditions of the Creative Commons Attribution (CC BY) license.

1. Introduction

The construction sector reportedly produces close to one-third of the world's greenhouse gas (GHG) emissions [1]. Reducing the environmental footprint of building materials is therefore a critical priority. In parallel, digital construction technologies, particularly extrusion-based 3D concrete printing (3DCP), are rapidly advancing [2–4]. This technology reduces manual labour, enables geometric freedom, and improves material efficiency. However, 3DCP imposes strict requirements on mix design: materials must exhibit rapid setting, sufficient early strength, controlled rheology, and long-term durability in the hardened state.

Gypsum–cement–pozzolan (GCP) systems represent a promising alternative binder concept. In standard Portland cement (PC) and gypsum mixtures without pozzolans,

ettringite formation can cause deleterious expansion and material destruction [5]. By combining gypsum with PC and pozzolanic additives, ternary composites can overcome the low green strength and poor water resistance typically associated with pure gypsum binders [6–8]. GCP binders benefit from early gypsum hydration and subsequent hydraulic hardening through cement hydration and pozzolanic reactions. The durability of GCP is provided by hydraulic hardening and the formation of stable compounds, including calcium hydrosilicates (C-S-H), calcium carbonates, and calcium sulfate dihydrate [8]. Notably, such systems allow a partial reduction in PC content, which is the most energy-intensive component of the composite (0.7–0.8 kg CO_2 per kg of CEM I 42.5) [9]. For sustainable 3DCP, reducing clinker content through supplementary cementitious materials or blended cements (e.g., CEM II or CEM III) is essential, and clinker reduction by at least 20% has already been achieved [10,11]. Previous studies on GCP composites have demonstrated that such systems can achieve up to approximately 40% reduction in carbon footprint compared to conventional PC-based materials, primarily due to clinker reduction and the utilisation of low-CO_2 gypsum and secondary materials, even despite embodied energy from metakaolin production at a calcination temperature of 700–800 °C [12–14].

Further optimisation can be achieved by incorporating mineral fillers and industrial by-products. Properly graded sand reduces binder consumption while maintaining structural buildability. Additional cement reduction may be possible through oil shale ash (OSA) or other mineral admixtures [15]. Moreover, the ternary approach enables the utilisation of secondary gypsum sources, including recycled plasterboard (construction and demolition waste (CDW)) and phosphogypsum (PG), a by-product of fertiliser production. Such valorisation supports circular economy principles and reduces environmental burdens.

Although alternative binders such as geopolymers, magnesia phosphate cement, and calcium sulfoaluminate (CSA) systems have been investigated for 3DCP [16], research on GCP-based materials for additive manufacturing remains limited. In particular, existing studies predominantly focus either on the mechanical performance of gypsum–cement blends under conventional casting conditions or on the rheology of cement-based 3DCP systems, without integrating systematic compositional optimisation, durability assessment, and printability requirements within a single experimental framework [17,18]. Moreover, there is a lack of comprehensive studies that (i) apply ternary-diagram optimisation to define quantitative compositional domains for 3D-printable GCP systems, (ii) compare primary and secondary gypsum sources in extrusion-based applications, and (iii) evaluate long-term moisture-induced deformation and freeze–thaw resistance in such composites. Durability is especially critical for gypsum-containing systems. Long-term exposure to moisture, freeze–thaw cycles, and aggressive environments may induce strength reduction and volumetric instability [8,19]. Water resistance is commonly evaluated through water absorption and the softening coefficient (ratio of wet to dry strength) [20,21]. While pure gypsum typically exhibits a softening coefficient below 0.5, incorporation of cement and pozzolan is expected to increase this value toward water-resistant levels (>0.80) [22]. In addition to short-term indicators, long-term deformation under water storage and frost resistance testing are necessary to assess performance under northern climatic conditions.

To date, no structured methodology has been proposed for the stepwise development of GCP binders specifically tailored to extrusion-based additive manufacturing, linking mix design parameters with rheological behaviour, mechanical strength evolution, and long-term durability. Therefore, the objective of this study is to develop durable and printable GCP compositions through a systematic, stepwise approach.

The novelty of this research lies in (i) the application of ternary-diagram optimisation to identify an optimal compositional domain for 3D-printable GCP binders; (ii) the comparative evaluation of diverse pozzolanic additives and secondary gypsum sources under

identical durability protocols; and (iii) the integration of rheological characterisation, in situ printability assessment, and long-term environmental performance within a unified experimental design.

This study therefore establishes a structured development framework for GCP binders in extrusion-based 3D printing, systematically linking ternary compositional optimisation with rheological behaviour, mechanical performance, and long-term durability. The results aim to define a quantitative design domain for low-carbon, printable GCP composites suitable for practical construction applications.

2. Materials and Methods

The development of 3D-printable GCP compositions was carried out using a stepwise experimental strategy, schematically presented in Figure 1. The research was structured into three consecutive iteration stages:

1. Stage I—Optimisation of ternary binder composition;
2. Stage II—Evaluation of alternative pozzolans and secondary gypsum sources with durability assessment;
3. Stage III—Adaptation of optimised compositions for extrusion-based 3D printing and rheological characterisation.

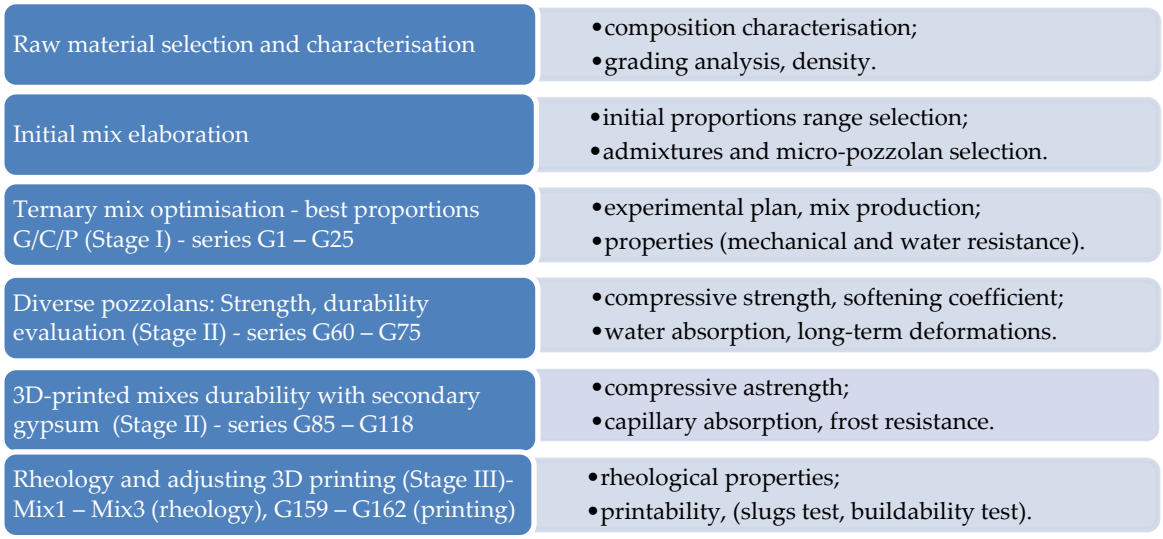

Figure 1. Step-by-step development scheme of GCP 3DP compositions.

This structured approach enabled progressive refinement of the material system, from fundamental compositional optimisation to full-scale printability verification.

2.1. Raw Materials

The primary binder components included building gypsum (BG), Portland cement (PC), and metakaolin (MK). Gypsum hemihydrate served as the rapid-setting component, while PC provided hydraulic hardening. Metakaolin is considered to modify the sulfate–aluminate balance and reaction kinetics, which may reduce the risk of expansive reactions associated with ettringite formation [17,20,23]. While selecting the raw materials for the GCP mixture, primarily local and commercially available components, as well as secondary materials derived from industrial by-product utilisation and recycling, are considered. The chemical composition was detected with a wavelength-dispersive X-ray fluorescence analyser (Thermo Fisher Scientific Inc., Denver, CO, USA).

Commercially available building gypsum (BG) (Knauf Latvija Ltd., Sauriesi, Latvia) was used as a reference gypsum. Its particle size was characterised by a broad granulometric distribution, with a d_{50} of 140 µm. The chemical composition of commonly used raw materials is summarised in Table 1. In this research, two types of secondary gypsum were used. The first one, i.e., the PG dihydrate sourced from Lifosa AB (Kėdainiai, Lithuania), was dried at 60 °C and milled using collision milling in a disintegrator to a d_{50} of 74 µm [13,19]. Subsequently, the calcium sulfate hemihydrate binder was produced by heating PG dihydrate powder at 145–150 °C for 4 h. The second one is recycled gypsum (RG) derived from the utilisation of plasterboard. The technological chain for obtaining a binder from secondary gypsum consists of sorting and collecting gypsum boards, thermal treatment at 145 °C, separation of the cardboard and subsequent crushing and collision milling in a disintegrator [23]. Compared to BG, RG may exhibit variability in chemical composition and impurity content due to differences in source material, contamination levels (e.g., paper residues), and prior hydration history. Such variability can influence setting kinetics, water demand, and interaction with cement and pozzolanic components. In the present study, RG was processed under controlled laboratory conditions (sorting, thermal treatment, and milling) to minimise variability; however, the potential influence of compositional fluctuations on mix performance should be considered when scaling the material for practical applications.

Table 1. Raw material chemical compositions.

	SiO_2	Al_2O_3	Fe_2O_3	CaO	MgO	SO_3	Na_2O	K_2O	TiO2	P_2O_5	LOI
BG	3.73	1.68	0.46	35.64	3.92	30.90	0.31	0.52	0.04		22.43
PG	1.07	0.70	0.22	37.16	0.21	37.38	0.48	0.11	0.10	0.57	19.24
PC	19.5	4.1	2.9	62.5	3.4	3.3	0.20	1.10			1.85
MK-40 Astra	57.30	35.73	2.04		0.23	0.13		0.43	1.69	0.04	1.81
OSA	1.26	3.35	3.35	37.48	4.43	6.42	0.16	3.37			<3
MKW waste	54.3	34.0	1.14	1.94	0.51	0.15	3.26	0.80	0.53		3.37
MK Metasil	51.2	23.3	0.90	4.87	1.6	0.12	12.2	0.56	0.23		
Z-50	68.0	12.2	1.3	4.0	0.9		0.75	2.8	0.20		
FA	50.8	27.5	6.43	2.89	1.33	0.65	0.60	2.22			

The change in structure is most likely due to the material's secondary use after hydration has already occurred. In detail, the technological scheme of the recycling process is described in previous works [13,24]. The chemical composition of RG has much greater variation, but the elemental composition is close to that of building gypsum. Compared to BG, RG and PG are characterised by fine grains and a more porous particle microstructure [13]. Granulometric curves of binding agents, micro- and macro-fillers, are shown in Figure 2.

Additionally, an inert fine aggregate was added to structure the mixture and reduce binder consumption. Natural quarry sand was used as a primary filling material. This is needed for mix stabilisation, forming the mix skeleton and decreasing the relative content of the binding agent. For initial iteration experiments, one sand type was used, provided by Sakret Latvia Ltd. (Ritvari, Rumbula, Latvia), with particle size up to 2 mm. For 3D printing, sand fractions 0/0.4 mm and a second sand Saulkalne S Ltd., Saulkalne, Latvia), 0.3/2.5 mm were used to improve the granulometric composition in the 3D-printed mixtures.

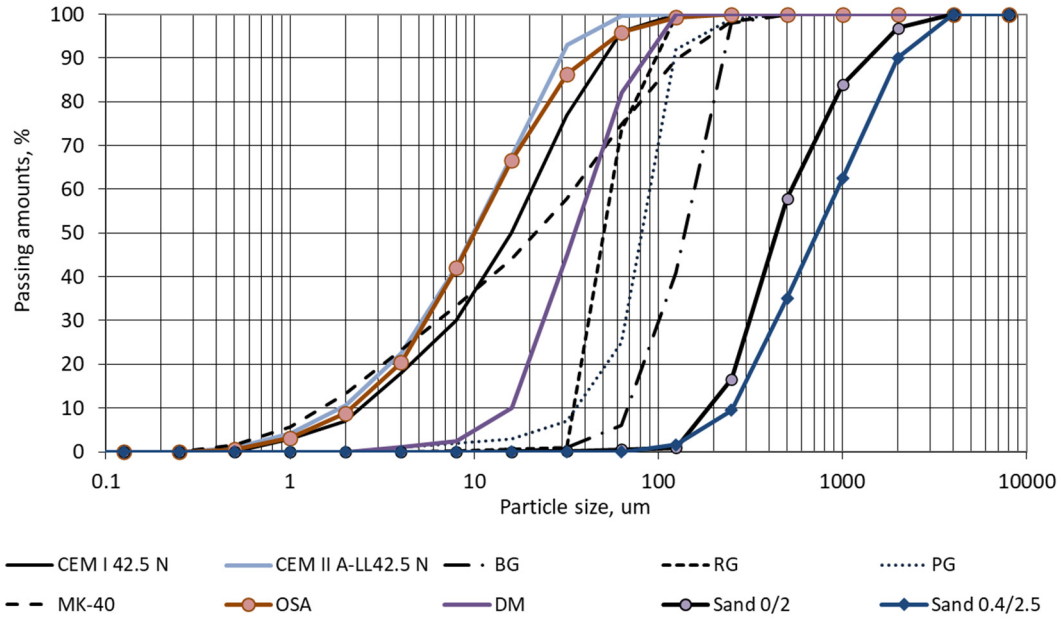

Figure 2. Binder and filler components' granulometric compositions.

It should be noted that without retardation, the GCP mixture has an extremely fast setting time. For Stage I and Stage II, plasticising and retarding additives were used separately. Gips Retard by TTK d.o.o. (Domžale, Slovenija), a powdered admixture intended to regulate gypsum setting time, was applied in an amount of 0.4% from binder in combination with plasticiser Stachement 115 by Stachema Polska (Świdnik, Poland) in an amount of 0.2% from binder. When adapting for 3D printing (Stage III), a complex additive was identified that served as both a plasticiser and a retarder Plasretard PE by Omya International AG (Oftringen, Switzerland), specifically designed for gypsum-containing mixtures. The quantities and names of the additives are shown in the tables defining the mixtures' compositions.

In the initial iteration, CEM I 42.5 N grade PC (Schwenk Latvia Ltd., Broceni, Latvia), Latvia) was used as a reference cement. However, in future experiments, the cement CEM II A-LL (Schwenk Latvia Ltd., Broceni, Latvia) was used as a more environmentally friendly solution. In this cement type, up to 20% of the clinker is replaced with limestone filler. In the secondary iteration, the possibility of using diverse pozzolanic admixtures was evaluated. Silica fume (SF), as one of the most popular pozzolanic additives, was used in this study (Elkem Microsilica®, Elkem ASA, Oslo, Narway). Nanosilica dispersion (NS) Levasil© CB 50 is derived from (Nouryon Ltd, Bohus, Sweeden, supplied by Telko Latvia Ltd.). Two local Si-Al oxide-containing by-products are used: (LM)-clay calcined in 750 °C (Lode quarry, Liepa, Latvia) and glass powder (GP) as a sheet glass recycling product (Priekulu Bloks, "Lejas Avoti", Vaive parish, Latvia). Tree types of metakaolin were used. One type of metakaolin (MKW) is a by-product of the expanded glass industry (Stikloporas Ltd., Druskininkai, Lithuania). Researchers have verified that this metakaolin exhibits good reactivity when combined with a cement binder [25]. Metakaolin Metasil (MK Metasil) (EKONRAD s.r.o., Brno, Czech Republic) and metakaolin Astra MK-40 (Astra Polska Ltd., Sękocin Stary, Poland) are commercial products for concrete production. Zeolite Zeobau 50 (Z-50) (Astra Polska Ltd., Sękocin Stary, Poland) is a silicate and aluminate additive for concrete that improves mechanical properties. The main mineral of the supplement is clinopatite with admixtures of Cristobalite and Plagioklaz. Dolomite powder (DM) was used as a micro filler (Saulkalne S Ltd., Saulkalne, Latvia). Fly ash (Kozienice, Poland, supplied by Schwenk Latvia Ltd.) was used as a pozzolanic admixture (FA).

In this work, OSA refers to oil shale fly ash collected from Eesti Elektrijaam (Vaivara, Estonia) and extracted from the flue gas stream using a novel integrated desulfurizer (NID). According to Hanžić et al. [26], this ash is characterised by relatively fine particles, mainly with smooth, globular morphology, and high CaO and SiO_2 contents.

For the final mix, MK was selected as the most appropriate admixture. MK was produced by the dehydration of a kaolin clay mineral ($Al_2(OH)_4Si_2O_5$). MK, a highly reactive aluminosilicate compound, was transformed into a dehydrated, amorphous state with the chemical formula $Al_2Si_2O_7$ after thermal treatment at 700–800 °C. In first iteration, commercially available MK-40 from Astra Polska Ltd. was used. Compositions of commercially available pozzolans are provided as a producer's datasheet. The general components of GCP composition used in this research are summarised in Figure 3.

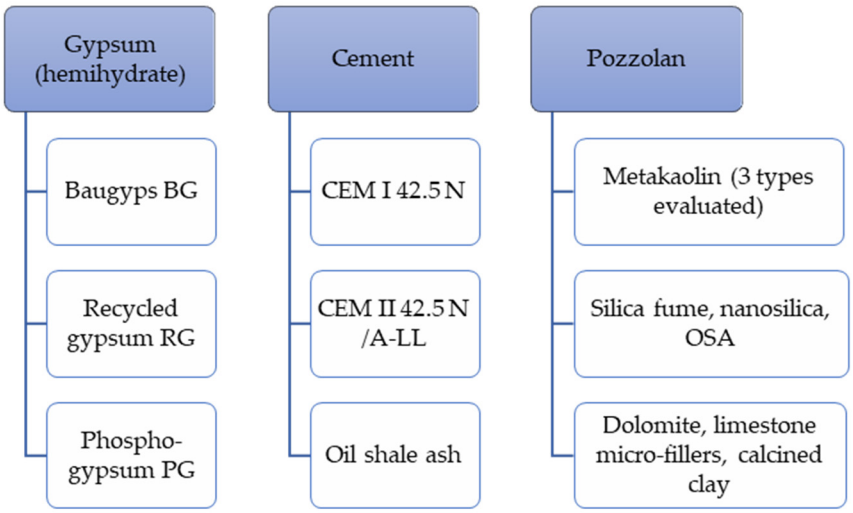

Figure 3. Raw materials used in GCP compositions.

2.2. Mix Preparation and Testing of Fresh Mix Properties

GCP compositions were prepared in laboratory conditions. Dry mineral components were dosed with ±1% accuracy and premixed before adding the liquid phase. Plasticiser and retarder admixtures were pre-dissolved in water and introduced during mixing to ensure uniform distribution. A planeatary 3 liter capacity laboratory mixer (Hobart Corporation, Troy, OH, USA) was used for mixture preparation, with a mixing time of approximately 3 min at 100–150 rpm. The water content was adjusted to achieve the required plastic consistency and workability suitable for extrusion-based processing.

Fresh-state properties were characterised using several complementary methods. Initial and final setting times were determined using a Vicat apparatus (Shanghai Civil & Road Instrument Co., Ltd., Shanghai, China) in accordance with EN 196-3 [27]. Workability was evaluated using the cone flow method according to EN 1015-3 [28]. Based on preliminary printing trials, an optimal flow diameter of approximately 160–180 mm after 15 jolts was identified as suitable for extrusion-based 3D printing.

The rheological behaviour of the fresh GCP mixtures was investigated using both vibration viscometry and rotational rheometry. Static viscosity measurements were conducted using a Vibro Viscometer SV-10 (A&D Company, Tokyo, Japan), which determines viscosity by monitoring the electrical current required to maintain resonance of sensor plates oscillating at 30 Hz with an amplitude below 1 mm. Fresh GCP paste yield stress and plastic viscosity were determined using a Rheotest RN 4.1 (Rheotest Medingen GmbH, Medingen, Germany) rotational rheometer equipped with a coaxial cylinder measuring system. The working element of the rheometer consists of an outer cylindrical measuring

cup with an internal diameter of 38 mm and a rotating cylinder rotor with a diameter of 35 mm. A gap of 1.5 mm is provided between them. Binder paste is placed inside the measuring cup and is sheared during the test. Measurements were performed under a stepwise shear protocol in which shear rate increased from 0 to 100 s^{-1} in ten increments, followed by a descending sequence from 100 to 0 s^{-1}. The ascending–descending shear protocol allowed evaluation of yield stress, plastic viscosity, and thixotropic behaviour relevant to extrusion-based 3D printing (Figure 4). Both binder pastes and sand-containing mixtures were tested on rheological performance.

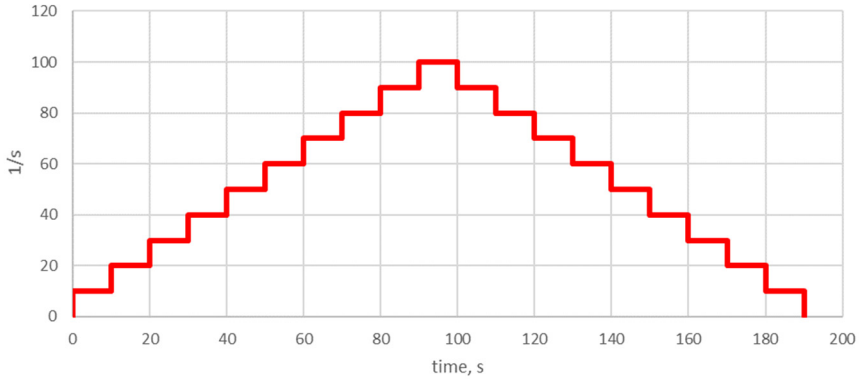

Figure 4. Rheometer work protocol.

The main rheological characteristics of 3D-printed mixtures are shear stress and viscosity, which can be determined using rheometric measurements. The simplest and most popular model for 3D printing mixtures is the Bingham model [29,30], defined by the following equation:

$$\tau = \tau_0 + \mu \gamma' \quad (1)$$

where τ is shear stress, τ_0 is yield stress, μ is plastic viscosity and γ' is the shear rate.

Printability and buildability were further assessed using adapted extrusion-based tests. The slug test was applied to estimate the plastic yield stress of the fresh mixture [31]. Yield stress (τ_c) was calculated from the mass of extruded material according to:

$$\tau_c = \frac{g \times m_s}{\sqrt[2]{3} \times S} \quad (2)$$

where $S = \pi R^2$ is the nozzle cross-sectional area, R is the nozzle radius, g is gravitational acceleration, $m_s = \rho S L_s$ is the slug mass, L_s is the slug length, and ρ is the fresh density of the extruded mixture. The yield stress reported later is the arithmetic mean of three measurements on the test sample.

Buildability (buckling test) was evaluated using a buckling test to determine the maximum number of layers that could be printed before structural collapse. These tests provided practical indicators of extrusion stability and structural integrity during printing. The buildability test was performed only once because it requires significantly more time, which can affect measurement accuracy.

2.3. Sample Preparation and Testing

For mechanical testing, cubic specimens (20 × 20 × 20 mm) were prepared during the initial and secondary experimental iterations. Prismatic specimens (40 × 40 × 160 mm) were produced for long-term deformation measurements. In deformation studies, steel pins were embedded at specimen ends. Specimens 100 × 100 × 50 mm were used for the frost resistance test. In the third stage, selected mixtures were adapted for extrusion-based

3D printing and evaluated after printing. It is recognised that size effects and anisotropy inherent to 3D-printed materials may influence mechanical performance; therefore, results obtained on cast specimens are primarily intended for comparative purposes and may overestimate the strength of printed elements [26,32].

After casting, the moulds were covered with plastic sheets to prevent moisture loss. The specimens were demoulded after 24–48 h and cured at 21 ± 1 °C and 95 ± 5% relative humidity until 28 days (or the age of testing). For long-term moisture exposure tests, samples after 28 days were stored in water at 21 ± 1 °C.

Before testing, the specimens were weighed and measured to determine density. Compressive strength was determined using a universal testing machine Zwick Z100 (ZwickRoell GmbH & Co., Ulm, Germany) in accordance with EN 196-1 [33]. Loading was applied at a rate corresponding to 0.5–1.0 mm/min. Strength was measured under three moisture conditions:

- Air-dry condition (f_{dry}), after drying at 50 °C for 24 h;
- Fully water-saturated condition (f_{wet}).

Average values were calculated from three specimens, and standard [34] deviations were determined to assess variability.

Water absorption (W) was calculated according to standard EN 1015-18 [35] as:

$$W = (m_{wet} - m_{dry})/m_{dry} \times 100\% \quad (3)$$

where m_{wet} and m_{dry} are the saturated and dry specimen masses, respectively.

Water resistance was evaluated using the softening coefficient:

$$K = f_{wet}/f_{dry} \quad (4)$$

Long-term dimensional stability under humid conditions was measured after one day, which was taken as the reference value. Specimens were initially cured in a high-humidity environment for 28 days and subsequently stored in water at 21 °C. Deformation measurements were performed using a digital displacement gauge with ±0.001 mm accuracy, and microstrains were calculated.

Freeze–thaw resistance was evaluated according to LVS CEN/TS 12390-9 (CF/CDF method), with adaptations [34]. Adaptations include: (i) the use of air cooling instead of liquid-based freezing; (ii) testing under water-saturated conditions without the addition of a de-icing salt solution; (iii) the use of prismatic plate specimens with dimensions of 100 × 100 × 50 mm instead of standard scaling specimens; and (iv) the use of plastic containers rather than standard steel containers. These adaptations were implemented to better represent the intended exposure conditions of GCP materials in non-de-iced environments and to ensure compatibility with the experimental setup. As a result, the obtained scaling values should be interpreted comparatively rather than as a direct classification according to EN 206 [36] exposure classes.

Additionally, separate 3D-printed elements were subjected to natural outdoor conditions for 9 months (from March to November).

Capillary water absorption was determined before freeze–thaw testing according to EN 772-11 [37]. Specimens (100 × 100 × 50 mm) cured for 28 days were partially immersed in water (by surface), and absorption values were expressed in g/dm^2.

2.4. 3D Printing Setup and Parameters

Experimental fabrication of GCP-based structures was carried out using a gantry-type additive manufacturing system developed at the 3DCP Laboratory of Riga Technical University, Faculty of Civil and Mechanical Engineering [38]. The system is supported by

mixers, pumps, and auxiliary equipment for printing structural elements. The experimental setup used in this study had a build envelope of 1500 × 1000 × 1000 mm. The extrusion system is based on a batch-type, auger-driven mechanism. Printing was performed using a 25 mm diameter round nozzle. The nozzle standoff distance (layer height) was maintained at approximately 10 mm. The extrusion rate ranged from 1.5 to 5 L/min, depending on mixture properties. The nozzle travel speed ranged from 10 to 60 mm/s. The resulting filament geometry was characterised by a width of approximately 40–50 mm, depending on the material behaviour. A more detailed description of the printing system, including hardware configuration and process control, is provided in [39].

2.5. Experimental Plan

2.5.1. First Iteration—Optimisation of GCP Composition

The task in this stage was to determine the range of optimal GCP additive proportions that yield the best physical and mechanical properties. Three GCP binder components were used: BG, PC, and MK (MK-40 from Astra Polska). Considering the results of initial mix testing and the analysed literature sources, the following ranges of variation in the mixture components were chosen: BG: 40–80%; PC: 0–50%; MK: 10–60%.

A ternary diagram was chosen to characterise the compositions of the covered mixtures. This system is convenient because each point in the diagram represents the original mixture, and the sum of the three components is 100%. The software OriginLab v.2024 [40] was used to describe the mixture compositions covered in this research. The experimental matrix (Figure 5) was designed as a structured, exploratory sampling scheme at constant gypsum levels. Contour plots were generated from interpolated measured data points and are intended to illustrate qualitative trends.

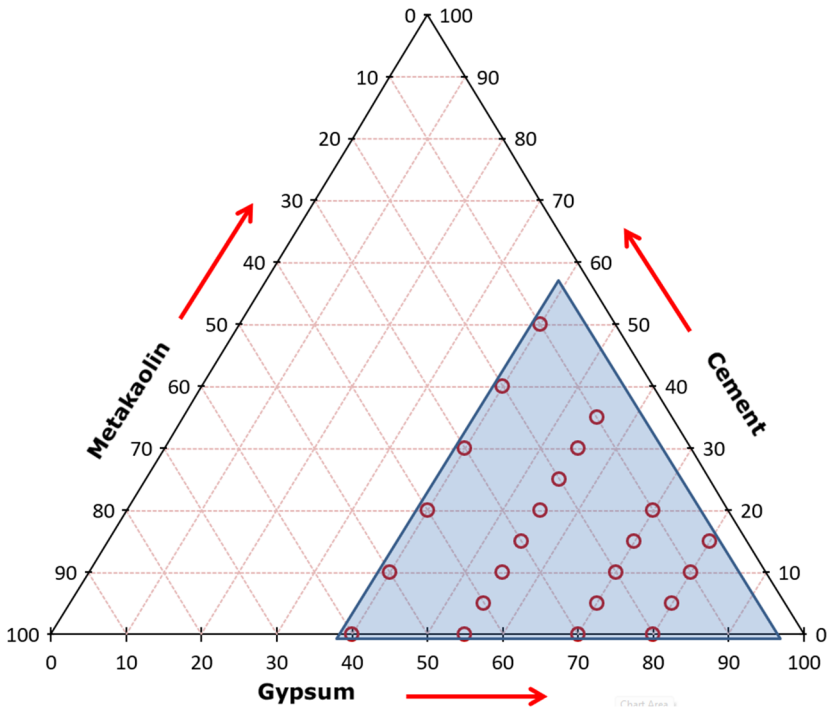

Figure 5. Ternary diagram of experimental points. The experimental range is coloured. Red circles are an experimental points.

It should be noted that water demand in the mixtures varied depending on the dry component ratios. As a result, water–binder ratios in the range 0.38–0.45 were selected to ensure the necessary mix workability (cone flow 160–180 mm). The effect of binder

composition on the water-to-binder ratio (W/B) was clearly observed. The lowest W/B values (0.38–0.40) were recorded for mixes G1–G6, with the lowest gypsum content (40%). In contrast, higher W/B values (0.42–0.43) were obtained for compositions G22–G25, G16, and G17, with high gypsum contents (70–80%). This trend can be attributed to the significantly higher water demand of gypsum compared to PC. The highest W/B ratios were observed in compositions G13–G17, which combine a relatively high gypsum content with a significant proportion of metakaolin. Thus, the water demand of the ternary binder system depends not only on the individual proportions of its components but also on their combined interactions.

The amount of retarder was chosen to ensure the setting time (which approximately corresponds to open print time) fell within the range of 20–40 min. A minimal dosage of plasticiser was chosen to provide a workable mix while preventing high flowability, which is undesirable for 3D printing.

Mechanical properties were tested at 7 days to determine early strength and at 28 days in wet (f_{wet}) and dry (f_{dry}) conditions. Water absorption (W) and the softening coefficient (K) were determined by testing the materials under moist conditions. The mass proportions of the compositions for the first iteration are shown in Table 2.

Table 2. Binder composition matrix of ternary gypsum–cement–metakaolin (GCP) mixtures used for initial optimisation (mass% of binder).

Mix	BG Gypsum (%)	CEM I (%)	MK Astra (%)	W/B	Plasticiser	Retarder
G1	40	50	10	0.39	0.20	0.40
G2	40	40	20	0.38	0.20	0.40
G3	40	30	30	0.38	0.20	0.40
G4	40	20	40	0.39	0.20	0.40
G5	40	10	50	0.40	0.20	0.40
G6	40	0	60	0.40	0.20	0.40
G7	55	35	10	0.41	0.20	0.40
G8	55	30	15	0.41	0.20	0.40
G9	55	26	19	0.41	0.20	0.40
G10	55	22.5	22.5	0.41	0.20	0.40
G11	55	19	26	0.41	0.20	0.40
G12	55	15	30	0.39	0.20	0.40
G13	55	10	35	0.43	0.20	0.40
G14	55	5	40	0.44	0.20	0.40
G15	55	0	45	0.45	0.20	0.40
G16	70	21	9	0.43	0.20	0.40
G17	70	16.5	13.5	0.43	0.20	0.40
G18	66.7	11.9	21.4	0.40	0.20	0.40
G19	66.7	7.6	25.7	0.40	0.20	0.40
G20	66.7	3.8	29.5	0.40	0.20	0.40
G21	66.7	0	33.3	0.40	0.20	0.40
G22	80	15	5	0.43	0.20	0.40
G23	80	10	10	0.42	0.20	0.40
G24	80	5	15	0.42	0.20	0.40
G25	80	0	20	0.42	0.20	0.40

2.5.2. Second Iteration—Optimisation of Alternative Pozzolans, Secondary Gypsum, and Durability Performance

Following the identification of the optimal compositional domain in the first iteration, the second stage focused on expanding the material system by incorporating alternative pozzolanic additives, secondary gypsum sources, and mineral fillers. The objective was to test durability performance while maintaining mechanical strength. The reference bench-

mark ternary composition established in Section 3.1 was retained, along with fixed binder proportions (gypsum/CEM/pozzolan = 55/22.5/22.5 mass%) and different pozzolanic materials. The mass proportions of the compositions for the second iteration are shown in Table 3, along with the corresponding water-to-binder ratios (W/B).

Table 3. Second iteration of GCP compositions with different pozzolanic materials.

Mix No.	Designation	Pozzolan Name	W/B	Plasticiser	Retarder
G60	MK	Astra MK-40	0.40	0.20	0.40
G61	Metasil	Metakaolin Metasil	0.42	0.20	0.40
G62	MKW	MKW (by-product)	0.42	0.20	0.40
G63	Z-50	Zeolite Zeobau 50 (Astra Polska)	0.42	0.20	0.40
G64	SF	Silica fume (Elkem)	0.53	0.20	0.40
G65	GP	Glass powder < 0.1 mm	0.41	0.20	0.40
G66	LM	Liepa clay calcined in 750 °C	0.42	0.20	0.40
G67	OSA	Oil shale ash	0.43	0.20	0.40
G70	FA	Fly ash (Korżienice)	0.42	0.20	0.40
G71	SF + DM	Silica fume + dolomite powder (1:3)	0.42	0.20	0.40
G72	DM	Dolomite powder	0.42	0.20	0.40
G73	NS + DM	Nanosilica sol. + dolomite powder (1:3)	0.42	0.20	0.40
G74	DM	Dolomite powder	0.34	0.20	0.40
G75	NS + DM	Nanosilica sol. + dolomite powder (1:3)	0.31	0.20	0.40

Various pozzolanic materials were evaluated, including metakaolin of different types, silica fume, zeolite Z-50, FA, calcined clay LM, and oil shale ash OSA.

Durability assessment included water absorption, determination of the softening coefficient, long-term moisture exposure, and freeze–thaw resistance testing. This stage enabled the identification of compositions suitable for further adaptation to extrusion-based 3D printing.

Subsequently, the GCP compositions with sand filler were tested for durability. These compositions were already close to 3D-printing conditions, contained sand filler, and used secondary gypsum as a gypsum component alongside BG. Gypsum was partially substituted with secondary gypsum materials, including PG and RG obtained from plasterboard CDW. Also, as a pozzolan component, OSA was used in combination with MK. The corresponding compositions are shown in Table 4.

Table 4. GCP compositions with sand for durability testing.

Mix	Reference Mixture	BG (%)	RG (%)	PG (%)	CEM (%)	MK (%)	OSA (%)	W/B	Plastretard PE (% from Binder)	Sand 0/2 mm (Mass % from Binder)
G85	G10	55	0	0	22.5	22.5	0	0.49	0.46	150
G95	G10	0	55	0	22.5	22.5	0	0.58	0.56	150
G102	G10	55	0	0	22.5	22.5	0	0.46	0.46	50
G104	G10	0	0	55	22.5	22.5	0	0.52	0.50	50
G105	G10	27.5	27.5	0	22.5	22.5	0	0.53	0.52	50
G107	G10	27.5	0	27.5	22.5	22.5	0	0.52	0.50	50
G108	G10	0	27.5	27.5	22.5	22.5	0	0.60	0.50	50
G109	G67	55	0	0	22.5	0	22.5	0.42	0.54	50
G110	G67	55	0	0	22.5	11.25	11.25	0.42	0.48	50
G118-3DP	G67	55	0	0	22.5	0	22.5	0.39	0.39	50

Additionally, the influence of mineral filler (sand) was assessed to reduce binder consumption and improve dimensional stability. The sand-to-binder ratio was typically varied between 0.5 and 1.5, depending on the required mechanical performance and

extrusion stability. It should be noted that composition 118-3DP was formulated based on composition G67 and tested for durability under naturally humid climatic conditions.

2.5.3. Third Iteration—Adaptation of GCP Compositions for 3D Printing

The third experimental iteration focused on adapting the previously optimised GCP compositions for extrusion-based 3D printing. Particular attention was devoted to controlling fresh-state properties and buildability to ensure stable extrusion, adequate open time, and the integrity of the printed element.

Based on the outcomes of the preceding optimisation stages, printable compositions were designed within the following binder composition ranges:

- Gypsum component (primary or secondary gypsum): approximately 38–55 wt.% of binder;
- PC (predominantly CEM II/A-LL type): approximately 10–25 wt.%;
- Pozzolanic additive (mainly MK or OSA): approximately 20–30 wt.%;
- Sand filler content corresponding to a sand-to-binder ratio of approximately 0.5–1.5.

Water-to-binder ratios were adjusted to 0.38–0.50 to ensure sufficient extrudability while maintaining the dimensional stability of printed layers.

Rheological behaviour was evaluated using a combination of flow table testing and in situ extrusion trials. The main parameters assessed included static and plastic viscosity, yield stress, extrusion continuity, and layer buildability. Selected compositions were subsequently validated by laboratory-scale 3D printing to confirm printability and structural integrity of the fabricated elements.

Three GCP compositions (Mix1–Mix3, with an optimum GCP proportion of 55/22.5/22.5) were additionally produced to evaluate the influence of the W/B ratio and inert filler content on the fresh mix rheological properties. Mix1 and Mix2 consisted of GCP binder paste containing limestone filler, while Mix3 additionally incorporated sand aggregate. The total sand content in these reference mixtures corresponded to approximately 140% of the mass of the binder paste. Due to the increased specific surface area of the sand particles, Mix3 required a higher water content than the paste-based mixtures.

Subsequently, a series of printable compositions (GCP159–GCP162) was developed using the optimised binder system, graded sand fractions, and admixtures suitable for extrusion-based manufacturing. These mixtures were characterised in terms of fresh density, yield stress, buildability, and short-term workability. The compositions investigated in this third iteration are summarised in Table 5.

Table 5. Mixture compositions investigated in the 3rd iteration (adaptation for extrusion-based 3D printing).

Component	Mix1	Mix2	Mix3	G159	G160	G161	G162
	Binder composition (mass % of binder)						
BG	55	55	55	55	55	27.5	38.2
PG	–	–	–	–	–	27.5	–
OSA	–	–	–	–	–	–	25.5
CEM type	CEM I	CEM I	CEM I	CEM II	CEM II	CEM II	CEM II
CEM (%)	22.5	22.5	22.5	22.5	22.5	22.5	10.8
MK (%)	22.5	22.5	22.5	22.5	22.5	22.5	25.5
	Water/Admixtures						
W/B	0.540	0.480	0.610	0.409	0.441	0.506	0.492
Plastretard PE	0.5	0.5	0.5	0.41	0.44	0.51	0.40

Table 5. *Cont.*

Component	Mix1	Mix2	Mix3	G159	G160	G161	G162
PP fibre	–	–	–	0.2%	0.2%	0.2%	0.2%
			Fillers/Aggregates				
Limestone filler	25	25	25	–	–	–	–
Sand 0/0.4 mm	–	–	–	25	70	70	70
Sand 0.4/2.5 mm	–	–	–	25	70	70	70
Sand 0/2 mm—sieved < 1mm)	–	–	175	–	–	–	–
Sand/Binder paste	–	–	1.4	0.5	1.4	1.4	1.4

3. Results

3.1. First Iteration: Optimisation of GCP Composition

The main results for the 25 mixture compositions are presented in Table 6. The influence of composition was evaluated using linear plots of four gypsum levels (40%, 55%, 70%, and 80%) (Figure 6), with regions of maximum strength highlighted. The density of the mixtures ranges from 1321 to 1789 kg/m^3. Higher-density mixtures (e.g., G2, G3, G9–G11) generally exhibit higher compressive strength compared to lower-density compositions with low cement content (e.g., G6, G14, G15).

Table 6. Test results of GCP matrix optimisation—28-day results.

Mix No.	ρ_o (kg/m^3)	f_{wet} (MPa)	f_{dry} (MPa)	K	W (%)
G1	1665 ± 18.0	24.3 ± 2.2	37.2 ± 2.7	0.65	12.8
G2	1737 ± 8.3	32.5 ± 1.5	46.8 ± 1.6	0.69	8.6
G3	1789 ± 16.3	35.7 ± 3.7	41.1 ± 3.5	0.87	4.8
G4	1664 ± 10.8	28.2 ± 0.8	39.4 ± 2.7	0.72	9.7
G5	1456 ± 22.8	11.8 ± 1.5	16.5 ± 2.2	0.72	23.3
G6	1385 ± 27.3	1.0 ± 0.0	2.6 ± 0.2	0.39	28.4
G7	1636 ± 1.1	18.9 ± 0.8	29.0 ± 1.1	0.65	9.4
G8	1612 ± 20.4	20.8 ± 0.6	27.2 ± 0.8	0.77	11.6
G9	1732 ± 18.3	32.1 ± 0.7	39.3 ± 1.9	0.82	6.0
G10	1678 ± 26.3	36.2 ± 0.7	42.6 ± 1.3	0.85	9.4
G11	1678 ± 27.0	35.2 ± 1.0	45.2 ± 0.6	0.78	7.7
G12	1601 ± 26.3	25.5 ± 2.1	34.1 ± 3.0	0.75	11.8
G13	1444 ± 10.0	14.6 ± 0.5	21.1 ± 1.2	0.69	22.1
G14	1370 ± 10.6	6.9 ± 0.5	12.0 ± 0.2	0.57	28.6
G15	1321 ± 9.4	1.4 ± 0.0	2.9 ± 0.2	0.47	24.5
G16	1548 ± 18.6	12.0 ± 1.1	17.5 ± 1.3	0.68	13.3
G17	1625 ± 14.9	16.4 ± 0.9	21.1 ± 1.6	0.78	7.9
G18	1620 ± 12.8	22.7 ± 1.2	28.0 ± 3.6	0.81	8.8
G19	1591 ± 25.4	12.4 ± 0.6	15.8 ± 1.7	0.79	12.7
G20	1516 ± 24.2	9.5 ± 0.5	11.8 ± 0.9	0.80	19.0
G21	1412 ± 13.6	3.0 ± 1.7	5.6 ± 0.3	0.54	14.6
G22	1467 ± 15.5	9.1 ± 0.9	19.0 ± 1.6	0.48	22.5
G23	1511 ± 11.7	16.0 ± 1.0	22.3 ± 0.7	0.72	19.5
G24	1454 ± 15.0	9.8 ± 0.7	15.6 ± 1.2	0.63	24.0
G25	1441 ± 4.2	3.6 ± 0.1	7.2 ± 0.6	0.50	21.2

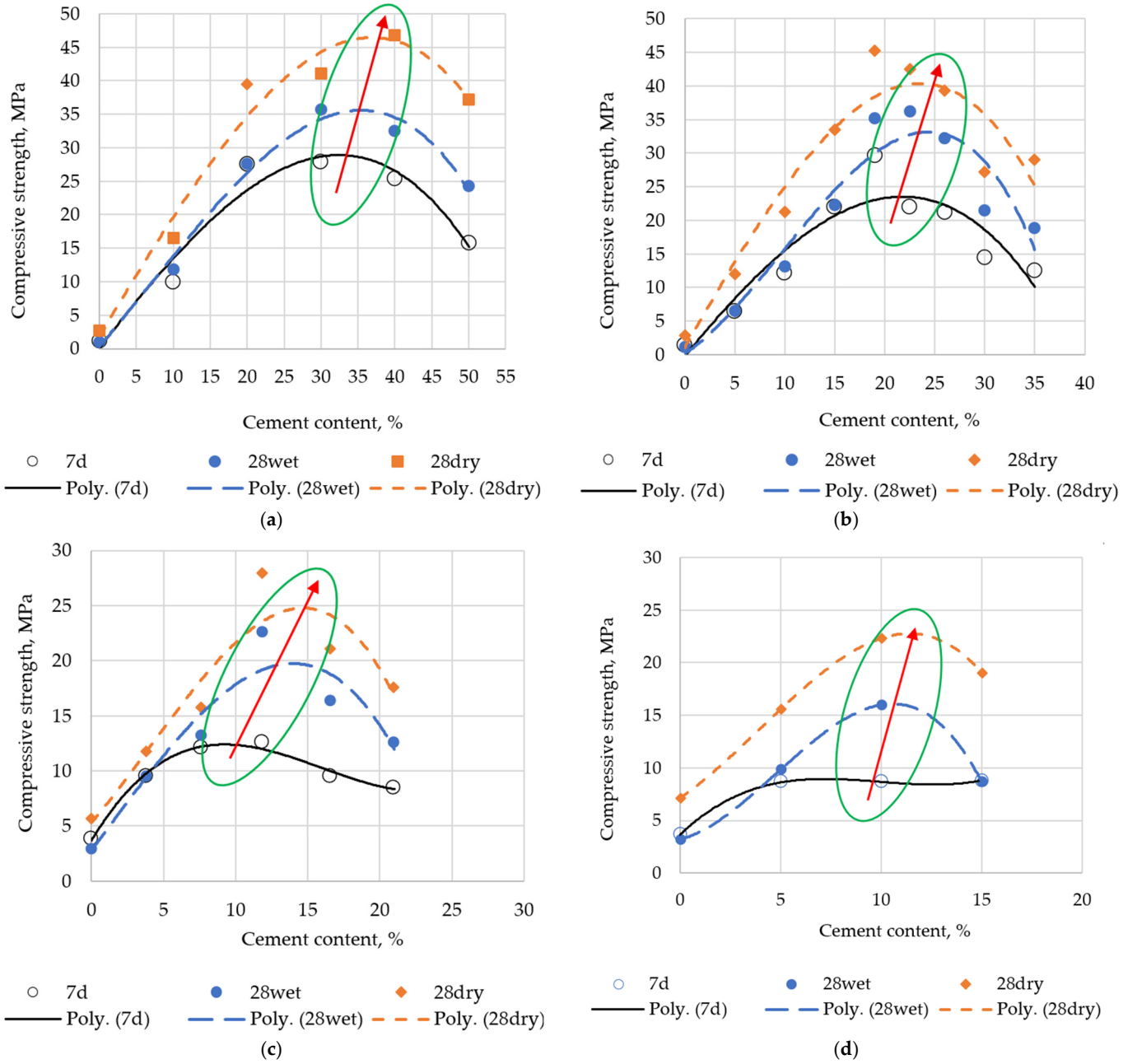

Figure 6. Compressive strength for different mix proportions. (**a**) Gypsum 40%; cement variation 0–50%; MK variation 10–60%. (**b**) Gypsum content 55%; cement variation 0–35%; MK variation 10–45%. (**c**) Gypsum content 70%; cement variation 0–22%; MK variation 10–35%. (**d**) Gypsum content 80%; cement variation 0–15%; MK variation 0–15%. The red arrow and green circle show the trend whereby at 28 days of curing, maximum strength is achieved with a higher cement content, compared to 7 days of curing.

At 28 days, the highest dry compressive strength values are recorded for mixtures G2 (46.8 MPa), G11 (45.2 MPa), and G10 (42.6 MPa). These mixtures also exhibit high wet compressive strength values (32–36 MPa). Lower strength values are observed for mixtures with higher gypsum content and lower cement content, such as G6, G14, and G15.

The softening coefficient (K) varies from 0.39 to 0.87. Higher values ($K \geq 0.80$) are observed for mixtures such as G3, G9, G10, G18, and G20, while lower values are associated with mixtures G6, G14, G15, and G22.

Water absorption ranges from 4.8% to 28.6%. The lowest values are observed in mixtures G3 (4.8%), G9 (6.0%), and G2 (8.6%), while the highest values are observed in mixtures G6 (28.4%) and G14 (28.6%).

The trends in strength development are illustrated in Figure 6. At low cement contents (≤10%), the difference between 7-day and 28-day compressive strength is limited. At higher cement contents, a more pronounced increase in strength between 7 and 28 days is observed.

The evolution of compressive strength as a function of cement content for different gypsum levels is presented in Figure 6a–d. Across all mixtures, a non-linear relationship between cement content and strength is observed, with a distinct optimum region rather than a monotonic increase. At low cement contents (≤10%), all compositions exhibit limited strength development, and the difference between 7-day and 28-day strength remains small, indicating that gypsum-dominated systems provide rapid but low ultimate strength. As cement content increases, a clear divergence between early-age (7-day) and later-age (28-day) strength becomes evident, reflecting the increasing contribution of cement hydration and pozzolanic reactions.

For mixtures with 40% gypsum (Figure 6a), compressive strength increases significantly with cement content, reaching peak values at approximately 35–45% cement. Beyond this range, a reduction in strength is observed, suggesting suboptimal binder balance and possible dilution of the gypsum-driven early structure.

At 55% gypsum (Figure 6b), a similar trend is observed, although the optimum shifts towards lower cement contents (~25–30%), indicating that increasing gypsum content reduces the required cement fraction for maximum performance while maintaining comparable strength levels.

For higher gypsum contents (70% and 80%, Figure 6c,d), the overall strength level decreases, and the optimum region becomes narrower and shifts further towards lower cement contents (~10–15%). In these systems, excessive gypsum limits long-term strength development, and the contribution of cement becomes insufficient to sustain higher strength gains.

Across all compositions, the 28-day dry condition consistently yields higher compressive strength than wet conditions, while the 7-day strength is less sensitive to curing state. The polynomial trendlines highlight that maximum strength is achieved within a relatively narrow compositional window, defined by a balanced proportion of gypsum, cement, and metakaolin.

To objectively analyse composition–property relationships, ternary diagrams were constructed to visualise the distribution of compressive strength and durability-related parameters within the gypsum–cement–metakaolin system (Figure 7a–c). The 7-day compressive strength distribution (Figure 7a) shows that early-age strength is predominantly governed by gypsum content, with higher strength values concentrated in mixtures containing approximately 45–60% gypsum and moderate metakaolin content. The influence of cement at this stage remains limited, resulting in a relatively broad but moderate-strength region. At 28 days under wet conditions (Figure 7b), the strength distribution becomes more localised, with a clear shift towards compositions containing increased cement content (approximately 20–30%) and balanced MK proportions. This indicates the growing contribution of cement hydration and pozzolanic reactions to strength development.

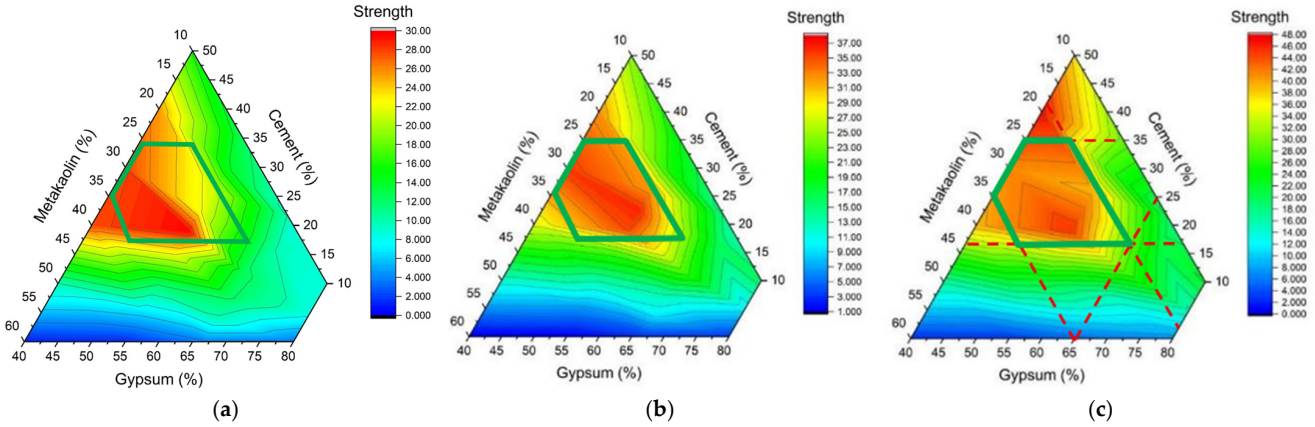

Figure 7. (**a**) Ternary diagram of compressive strength for 7-day samples. (**b**) Ternary diagram of compressive strength for 28-day wet samples. (**c**) Ternary diagram of compressive strength for 28-day dry samples. A green line borders the optimal area. The red dashed lines show the coordinates of the gypsum, cement and metakaolin content for the optimal area.

Under dry conditions (Figure 7c), the compressive strength reaches its maximum values, and a well-defined optimal region emerges. This region, highlighted in green, is centred on compositions containing approximately 50–60% gypsum, 20–30% cement, and 20–35% metakaolin. The contraction of high-strength zones compared to the 7-day results indicates increased sensitivity of performance to compositional balance at later ages.

The ternary diagrams of the water absorption and softening coefficient for 28-day samples are presented in Figures 8a and 8b, respectively, providing insight into the durability-related behaviour of the GCP system.

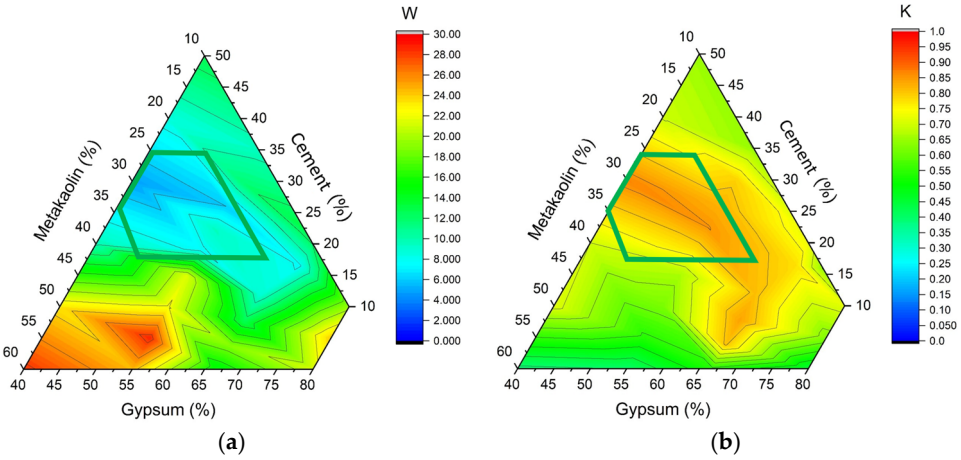

Figure 8. (**a**) Ternary diagram of water absorption for 28-day samples. (**b**) Ternary diagram of softening coefficient K for 28-day samples. A green line borders the optimal area.

The water absorption distribution (Figure 8a) shows a strong dependence on gypsum content. Mixtures with high gypsum proportions (>65%) exhibit significantly higher water absorption, indicating a more porous, less dense microstructure. In contrast, lower absorption values are observed in compositions with moderate gypsum content (approximately 50–60%) and balanced cement and metakaolin fractions. The region of reduced water absorption corresponds closely to the compositional range identified as optimal in the strength analysis.

The softening coefficient K (Figure 8b) demonstrates a similar compositional trend, with higher values (indicating improved resistance to water-induced strength loss) concentrated within the same optimal region. Mixtures with excessive gypsum content exhibit

reduced K, reflecting increased susceptibility to moisture-related degradation. Conversely, compositions with balanced binder proportions maintain higher stability, with K values approaching 0.8–0.9.

Based on these results, mixture G10 (55/22.5/22.5) was selected as a benchmark composition for further experimental investigation. This comparison provides a combination of high compressive strength (36.2 MPa), a high softening coefficient (K = 0.85), and moderate water absorption while maintaining a relatively low cement content. This balance between mechanical performance, durability indicators, and clinker reduction was considered optimal for further development. Among the compositions located within the optimal ternary domain, several mixtures (e.g., G9, G10, and G11) demonstrated comparable mechanical performance.

3.2. Second ITERATION: The Effect of Diverse Binder Compounds

3.2.1. Compressive Strength of Mixtures with Different Pozzolans

The benchmark GCP composition (55/22.5/22.5) was used as the reference mixture. Various pozzolanic admixtures were incorporated, including metakaolin (MK, Metasil, MKW), Z50, SF, NS, recycled glass powder (GP), fly ash (FA), calcined clay (LM), OSA, and dolomite powder (DP). The compressive strength results at 7 and 28 days are presented in Figure 9, and additional properties are summarised in Table 7. For all compositions, the highest strength values were obtained in the dried state. Among the tested mixtures, metakaolin-based compositions (G60–G62) exhibited the highest 28-day wet compressive strength, ranging from 26.8 MPa to 32.2 MPa. Zeolite (G63) and silica fume (G64) also showed comparable performance, with strengths of 23.3 MPa and 19.8 MPa, respectively. Mixtures containing recycled glass (G65), calcined clay (G66), and fly ash (G70) showed lower compressive strength. Dolomite-based compositions (G72–G75) also exhibited comparatively low strength values.

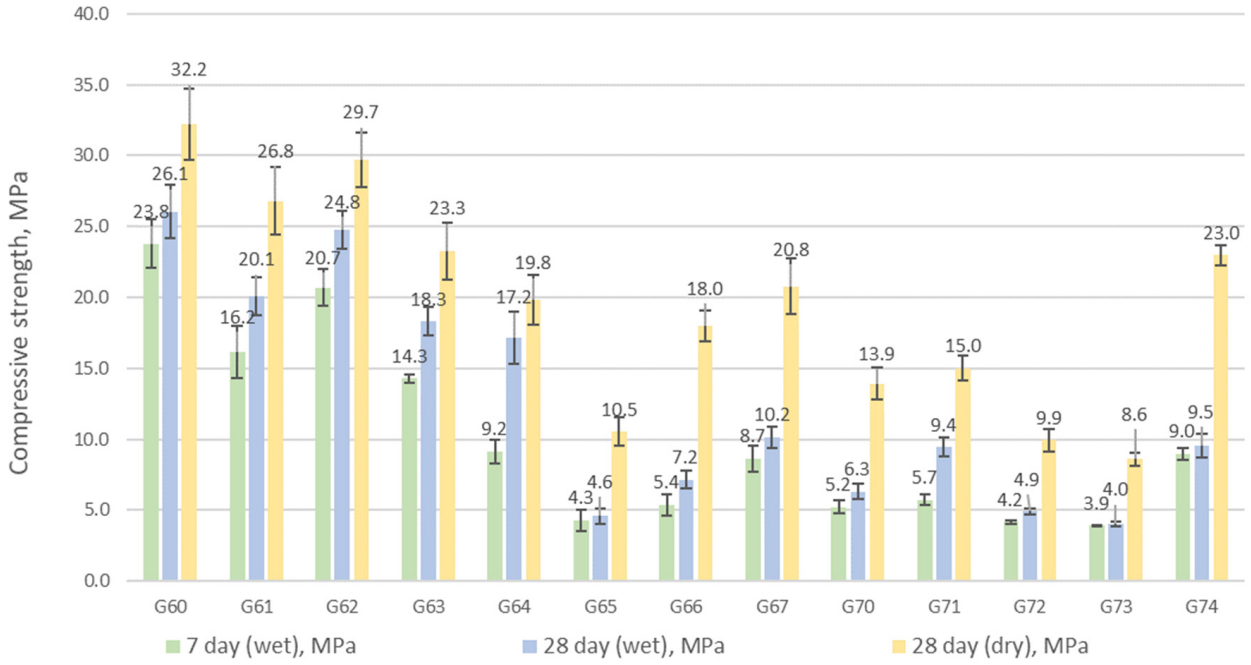

Figure 9. The effect of different pozzolanic components on compressive strength.

Table 7. GCP compositions and properties.

Mix No.	Pozzolan Type	Pozzolan Name	W/B	Wet Density (kg/m^3)	Dry Density (kg/m^3)	Δρ (kg/m^3)	Softening Coefficient (K)	Water Absorption (%)
High durability (K ≥ 0.75)								
G60	MK	MK-40 Astra	0.40	1800 ± 39.7	1656 ± 12.3	144	0.81	10.9 ± 1.20
G61	MK	Metasil	0.42	1701 ± 30.9	1523 ± 27.0	178	0.75	13.7 ± 0.69
G62	MK	MKW	0.42	1726 ± 32.1	1572 ± 13.7	154	0.83	12.0 ± 0.38
G63	Z-50	Zeobau 50	0.42	1732 ± 23.1	1523 ± 14.9	209	0.79	15.3 ± 0.52
G64	SF	Elkem	0.53	1626 ± 30.0	1342 ± 34.7	284	0.87	21.3 ± 0.79
Moderate durability (0.60 ≤ K < 0.75)								
G71	SF + DM	SF + DM (1:3)	0.42	1809 ± 21.8	1472 ± 10.8	337	0.63	24.2 ± 0.60
Low durability (K < 0.60)								
G72	DM	Dolomite	0.42	1807 ± 23.5	1463 ± 10.4	344	0.50	24.7 ± 0.82
G67	OSA	Oil shale ash	0.43	1791 ± 25.3	1488 ± 21.9	303	0.49	22.1 ± 1.07
G73	NS + DM	Nanosilica sol. + DM (1:3)	0.42	1709 ± 24.4	1324 ± 13.6	385	0.47	30.5 ± 0.69
G70	FA	Fly ash (Korżienice)	0.42	1735 ± 31.7	1410 ± 10.2	325	0.45	24.1 ± 0.49
G65	GP	Glass powder (<0.1 mm)	0.41	1738 ± 33.5	1437 ± 17.1	301	0.44	23.0 ± 0.84
G66	LM	Calcined Liepa clay (750 °C)	0.42	1750 ± 21.0	1447 ± 8.3	303	0.40	22.3 ± 0.76
G74	DM	Dolomite	0.34	1949 ± 17.9	1622 ± 9.9	327	0.41	20.9 ± 0.34
G75	NS + DM	Nanosilica sol. + DM (1:3)	0.31	1910 ± 23.3	1568 ± 13.3	342	0.39	22.8 ± 0.68

Water resistance indicators (softening coefficient and water absorption) are summarised in Table 7. Mixtures with higher compressive strength generally exhibited higher softening coefficients and lower water absorption.

3.2.2. Long-Term Dimensional Stability

The development of micro-deformation during long-term water curing is presented in Figure 10a,b. Metakaolin-based systems (G60–G62) exhibited initial strains of 2.5–4 mm/m, followed by stabilisation over time. The zeolite-based mixture (G63) showed lower initial strain (1–1.5 mm/m) and stable behaviour. Silica fume (G64), fly ash (G70), and the combined silica fume–dolomite system (G71) demonstrated low deformation levels (<2 mm/m) with no significant increase over time.

In contrast, mixtures containing glass powder (G65), calcined clay (G66), and OSA (G67) exhibited progressive deformation leading to failure. G66 showed continuous strain development reaching approximately 8×10^{-3} mm/m at ~200 days. G67 exhibited slower but continuous strain growth until failure. G65 showed delayed acceleration of deformation.

Dolomite-based systems (G72–G75) exhibited low initial strain followed by progressive increase. Mixtures G72 and G73 showed rapid increases in deformation and failure, whereas G74 and G75 (with lower W/B ratios) exhibited slower, continuous strain development.

Cracking patterns after long-term exposure are shown in Figure 11. Cracking was observed to be localised, with different mixtures exhibiting varying degrees of damage. Compositions G72 and G73 were destroyed within approximately one year.

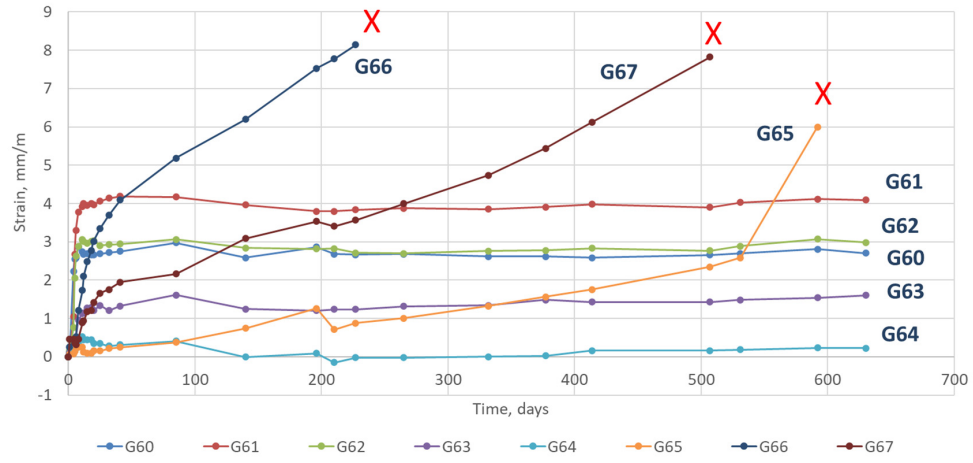

(**a**)



(**b**)

Figure 10. Long-term moisture performance test. X—sample destruction. (**a**) samples G60–G67; (**b**) samples G70–G75.

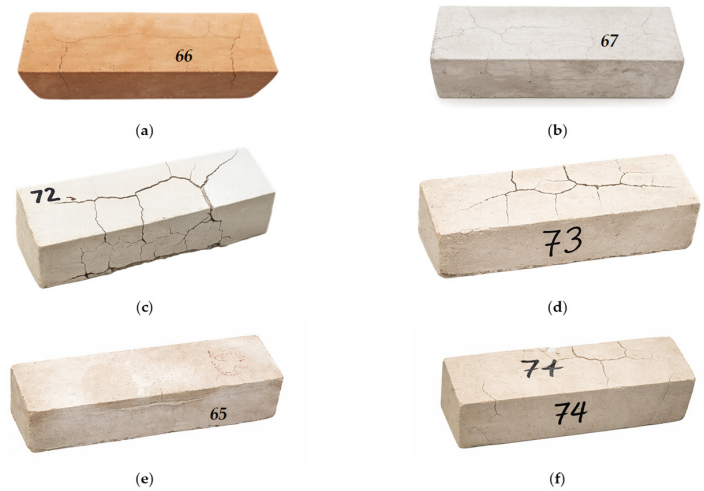

Figure 11. GCP samples after long-term water curing exhibit swelling-induced cracking. (**a**) G66–extensive cracking after ~210 days; (**b**) G67—distributed crack network after ~265 days; (**c**) G72—complete structural degradation (~371 days); (**d**) G73—pronounced cracking after ~190 days; (**e**) G65—initial cracking with delayed deformation (>350 days); (**f**) G74—moderate cracking after prolonged exposure (~500 days).

3.2.3. Frost Resistance

The physical and durability-related properties are summarised in Table 8, while the corresponding compressive strength development of the selected GCP compositions is presented in Figure 12. The wet density of the mixtures ranges from 1812 to 1992 kg/m^3, while dry density varies from 1556 to 1767 kg/m^3. The highest densities are observed for mixtures G85, G95, and G109, whereas lower values are recorded for G108 and G104. At 7 days (wet conditions), compressive strength values range from 9.5 MPa (G109) to 24.8 MPa (G102). Most mixtures fall within the range of 18–25 MPa (compositions G102, G104, G105, and G107), exhibiting the highest early-age strength. At 28 days (wet conditions), compressive strength increases across all mixtures, reaching values between 13.6 MPa (G109) and 34.5 MPa (G102). Higher strength values are observed for mixtures G102, G107, and G95, while G109 and G110 show comparatively lower performance. Under dry conditions at 28 days, compressive strength further increases, with values ranging from 33.4 MPa (G109) to 43.4 MPa (G102). The highest strengths are recorded for G102, G107, and G95, all exceeding 38 MPa. The difference between wet and dry strength is observed for all mixtures. The softening coefficient (K) varies from 0.41 to 0.84. Higher values are observed for mixtures G107 (0.84), G95 (0.80), and G102 (0.79), while lower values are recorded for G109 (0.41), G118-3DP (0.43), and G110 (0.60). Water absorption ranges from 10.5% to 18.6% for the tested compositions. The lowest values are observed for G102 (10.5%), G110 (11.1%), and G105 (12.1%), while higher values are recorded for G108 (18.6%) and G104 (15.3%). The 3D-printed mixture (G118-3DP) exhibits compressive strength values comparable to those of lower-performing cast mixtures, with a reduced softening coefficient (0.43) and moderate water absorption (13.8%).

Table 8. GCP compositions' physical properties.

Mix Designation	Wet Density (kg/m^3)	Dry Density (kg/m^3)	Softening Coefficient	Water Absorption (%)
G85	1992 ± 30.0	–	0.73	–
G95	1975 ± 41.0	1767 ± 30.6	0.80	12.3 ± 0.54
G102	1905 ± 16.3	1735 ± 13.6	0.79	10.5 ± 0.38
G104	1895 ± 22.8	1643 ± 25.8	0.77	15.3 ± 2.03
G105	1831 ± 17.4	1642 ± 15.0	0.77	12.1 ± 0.36
G107	1864 ± 28.6	1650 ± 12.5	0.84	14.7 ± 0.49
G108	1812 ± 33.5	1556 ± 8.8	0.71	18.6 ± 0.56
G109	1958 ± 18.3	1722 ± 10.0	0.41	14.7 ± 0.24
G110	1906 ± 22.4	1738 ± 2.6	0.60	11.1 ± 0.43
G118-3DP	1939 ± 37.2	1739 ± 14.5	0.43	13.8 ± 0.13

The evolution of capillary water absorption over time for the selected GCP compositions is presented in Figure 13. All mixtures exhibit a rapid initial increase in absorption within the first hours, followed by a gradual reduction in absorption rate and a tendency towards stabilisation at longer times. Significant differences in both absorption rate and total absorbed water are observed between the mixtures. The highest capillary absorption values are recorded for mixtures G104, G109, and G108, which reach approximately 60 g/dm^2, 55 g/dm^2, and 54 g/dm^2, respectively, after 48 h. These mixtures also show the steepest initial absorption rates. Intermediate behaviour is observed for mixture G95, reaching approximately 39 g/dm^2 after 48 h. Mixtures G85, G107, G105, and G110 exhibit lower capillary absorption, with final values ranging from approximately 25 to 30 g/dm^2. The lowest capillary absorption is observed for mixture G102 (benchmark composition with 50% sand), which remains below 7 g/dm^2 throughout the entire test period and shows a significantly slower absorption rate compared to all other compositions.

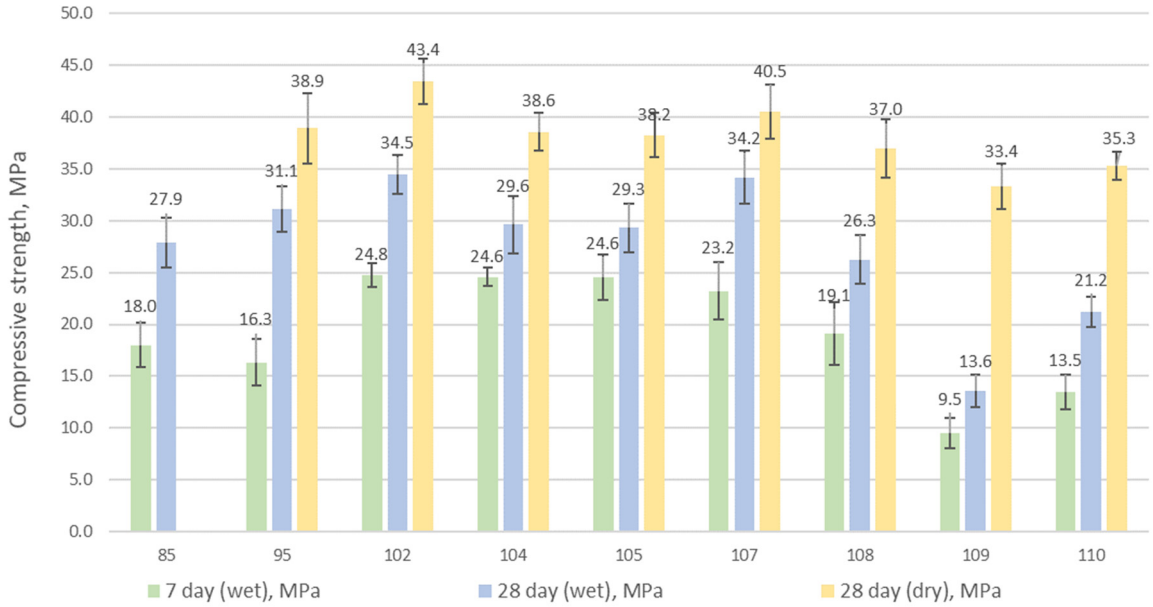

Figure 12. GCP composition compressive strength.

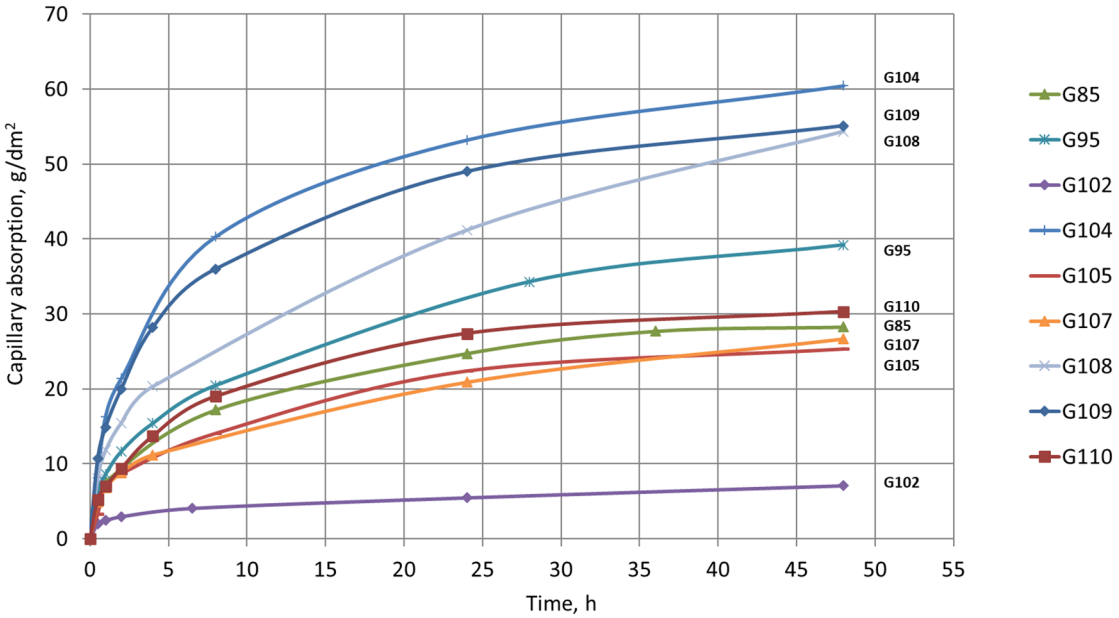

Figure 13. The charts of capillary water absorption.

The surface scaling values of different GCP compositions after exposure to freeze–thaw cycles are presented in Figure 14. Visible differences in surface integrity are observed between the tested compositions, indicating varying resistance to scaling. Mixtures G104, G109, and G108 exhibit pronounced surface deterioration and show the most severe scaling damage, approaching 2000 g/m^2. Intermediate behaviour is observed for mixtures G85, 95, 107 and G110, where surface degradation is present but less extensive, with partial retention of structural integrity and moderate surface scaling. Significantly, two compositions demonstrate the highest frost scaling resistance: G102, the benchmark mix, and G105, a BG + RG combination with a sand content of 50%. Differences are also observable in the uniformity of damage distribution, from localised defects to more widespread surface deterioration.

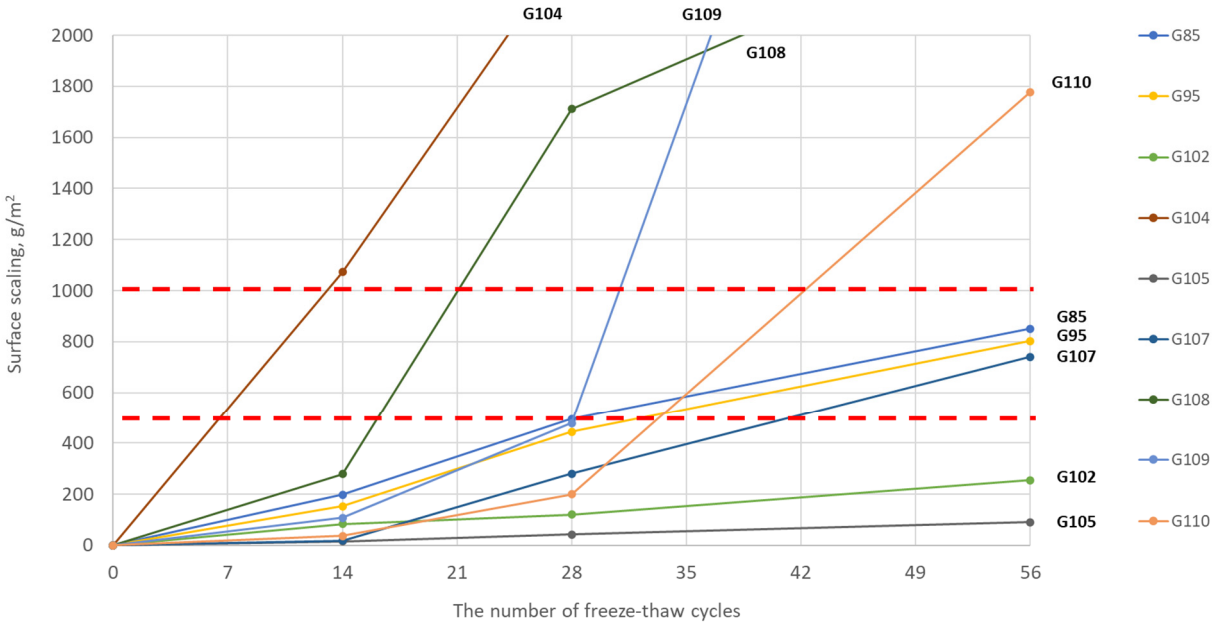

Figure 14. Surface scaling of 3DP adopted GCP compositions. Red dotted lines represent scaling compliance criterion, which correspond to acceptable (1000 g/m^2) and good (500 g/m^2) scaling resistance in accordance with [41].

The condition of the 3D-printed composition G118-3DP after outdoor exposure is presented in Figure 15. After the standard 28-day curing period, the uncovered samples were subjected to natural outdoor climatic conditions for 9 months (March to November). The following average variations in climatic parameters occurred: temperature (0–26 °C), relative humidity (50–97%), and cumulative precipitation up to 550 mm. After 7 months of exposure, visible cracking is observed along the printed layers, with both vertical and horizontal cracks indicating a loss of structural continuity. The cracks are predominantly aligned with the layer interfaces and extend through multiple deposited layers.



Composition No G118-3DP: after 7 months (cracking); after 9 months (destroyed).

Figure 15. Outdoor test for 3D-printed composition No. 118-3DP.

After 9 months of exposure, the specimen exhibits severe degradation and loss of structural integrity. The printed element is fully fragmented, with the original geometry completely collapsed. The results demonstrate a progressive deterioration of the 3D-printed structure under outdoor conditions, transitioning from initial cracking to complete structural failure over the exposure period.

3.3. Third Iteration—Rheological Characterisation of GCP Composition for 3D Printing

The rheological behaviour of the developed GCP mixtures was evaluated using vibration viscometry and rotational rheometry. Three compositions (Mix1–Mix3) with varying W/B ratios and aggregate content were analysed. It should be noted that in Mix3, the sand was presifted through a 1 mm mesh sieve because the distance between the cylinders in the rheometer is 1 mm.

Static viscosity was investigated using the Vibro Viscometer SV-10. The evolution of static viscosity for the three compositions is shown in Figure 16. The lowest initial viscosity (~370 mPa·s) was observed for Mix1, corresponding to the highest W/B ratio. Mix2 and Mix3 exhibited higher initial viscosities (~1300 mPa·s).

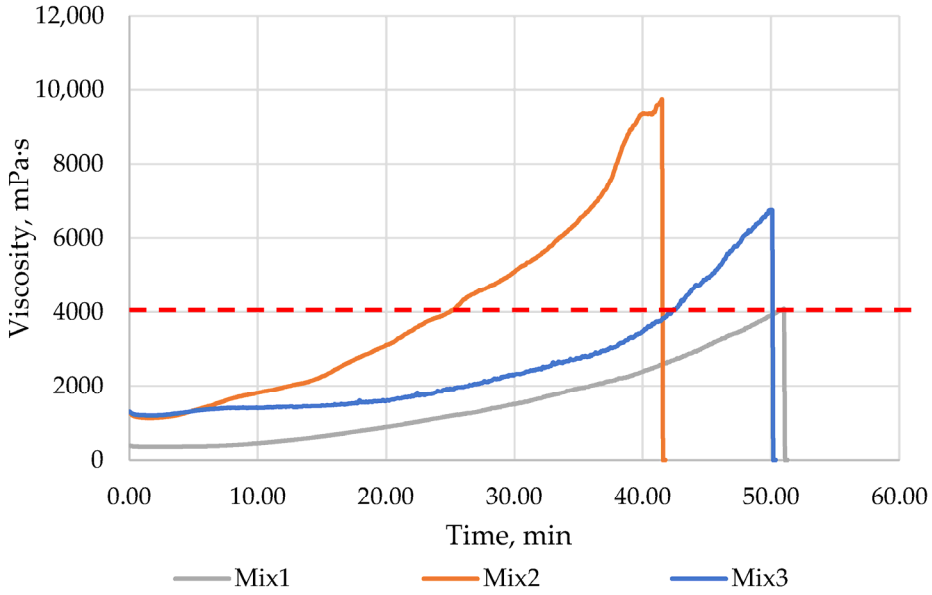

Figure 16. Static viscosity curves. Red dashed line indicates the maximum viscosity value when the mixture becomes rigid and unsuitable for 3D printing.

At static viscosity values greater than 4000 mPa·s, the mix becomes quite stiff and unsuitable for extrusion. Taking into account this limit, the estimated open print times are:

- Mix1: ~50 min;
- Mix2: ~25 min;
- Mix3: ~42 min.

The higher viscosity observed in Mix3 is attributed to the presence of a mineral aggregate, which increases internal friction and reduces the amount of free water and binder paste available for flow. Mix2 shows similar behaviour due to its lower W/B ratio compared to Mix1.

Shear stress and plastic viscosity were measured using a rotational rheometer. The Bingham model was chosen as the simplest and most suitable option to characterise the rheological behaviour of the GCP mixture, as described by Equation (1). The rheological curves on the descending section 100–0 s^{-1} were approximated using a linear function that defines the value of plastic viscosity μ and yield stress τ_o as the intersection with the Y axis. The rheological parameters derived using the Bingham model are summarised in Table 9.

Table 9. Rheological property summary.

	Mix1	Mix2	Mix3
RHEO, 5 min.			
Yield stress, Pa	189	300	345
Shear stress, Pa	64	112	195
Plastic viscosity, mPa·s	670	830	6300
Static viscosity, mPa·s	370	1300	1300
RHEO 30, min.			
Yield stress, Pa	220	418	380
Shear stress, Pa	67	114	225
Plastic viscosity, mPa·s	670	925	8920
Static viscosity, mPa·s	1510	5100	2300

The rheological curves for Mix1 and Mix2 (Figures 17 and 18) demonstrate a stable decrease in viscosity with increasing shear rate. At 5 min, the mixture exhibited a lower yield stress than at 30 min, indicating time-dependent structuration. For Mix1, yield stress increased from 189 Pa to 220 Pa over time (Table 9), while plastic viscosity remained approximately constant (670 mPa·s). Mix2 exhibited similar behaviour (Figure 18), with higher yield stress and plastic viscosity compared to Mix1. At 30 min, yield stress increased from 300 Pa to 418 Pa. Plastic viscosity increased slightly (830 to 925 mPa·s). Mix3 (Figure 19), containing sand, showed a different rheological response. Shear resistance increased with rotational speed, and the yield stress ranged from 345 Pa to 380 Pa. Plastic viscosity was significantly higher than that of the paste mixtures, reaching 6300 mPa·s at 5 min and 8920 mPa·s at 30 min.

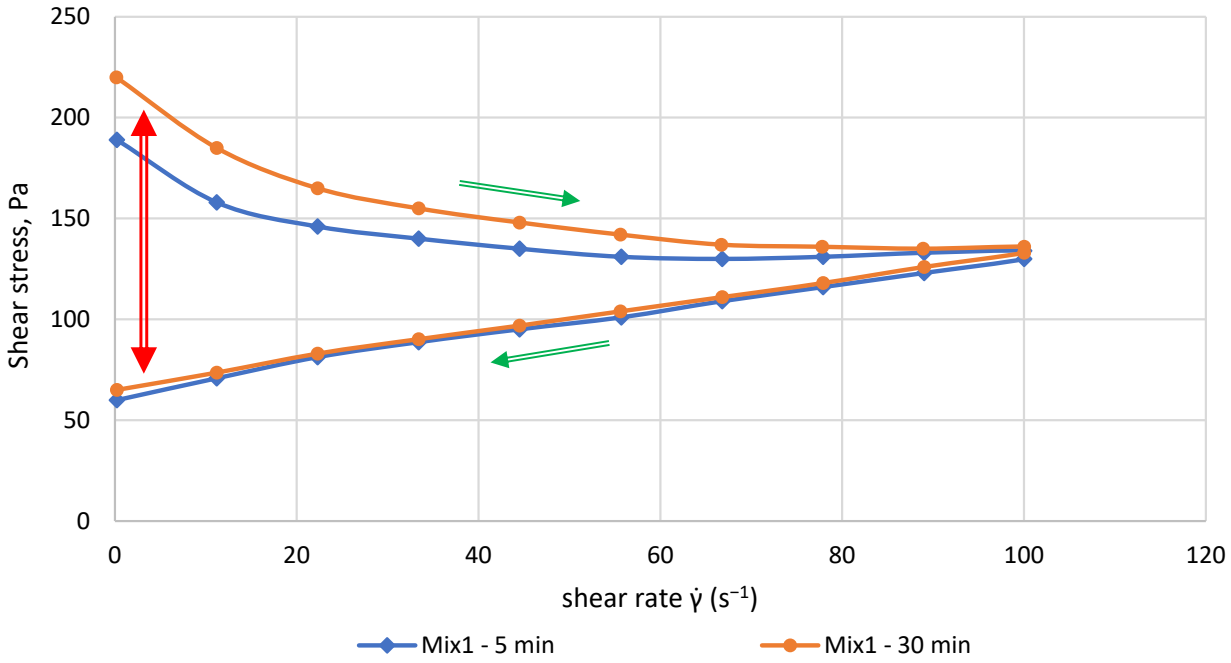

Figure 17. Mix1 rheometry chart after 5 and 30 min. The red arrow shows the difference between yield stress and shear stress, which can characterise the mix thixotropy. Green arrows show the trend of shear stress changes with increasing and decreasing shear rate. The red arrow characterizes thixotropy.

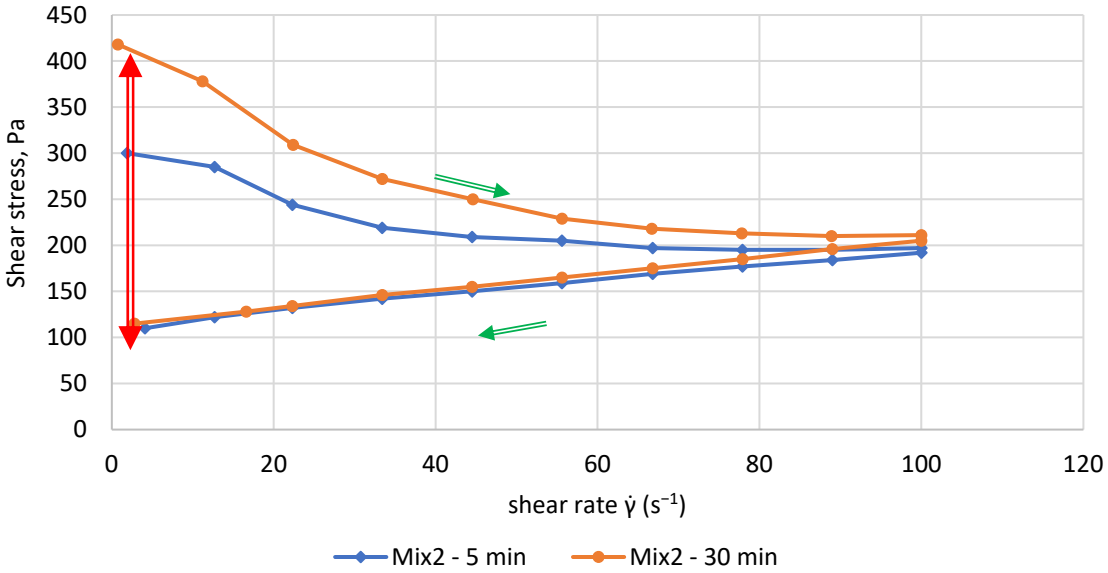

Figure 18. Mix2 rheometry chart after 5 and 30 min. Green arrows show the trend of shear stress changes with increasing and decreasing shear rate. The red arrow characterizes thixotropy.

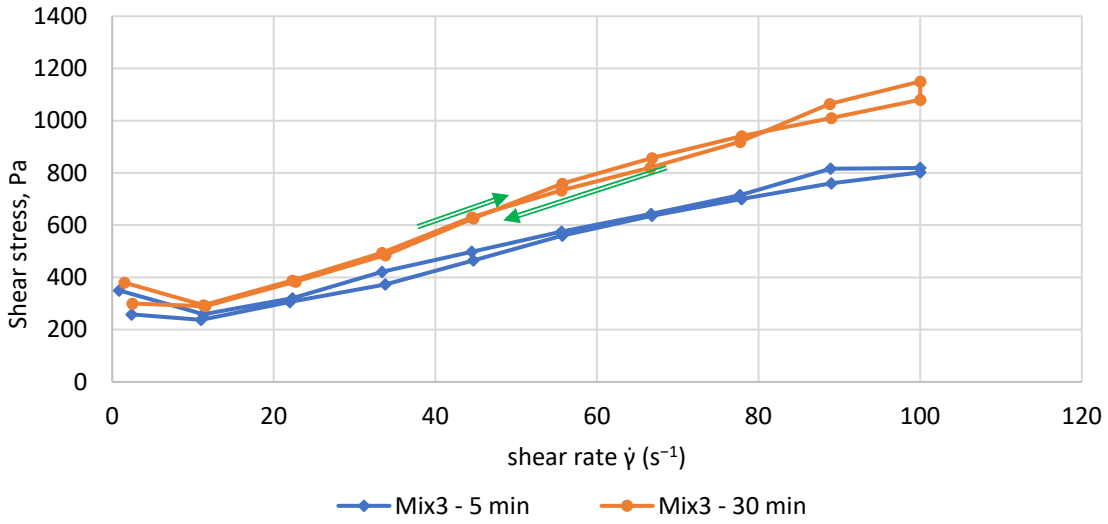

Figure 19. Mix3 rheometry chart after 5 and 30 min. Green arrows show the trend of shear stress changes with increasing and decreasing shear rate.

3.4. Adoption for 3D Printing

Full-scale GCP mixtures were produced and tested under practical 3D printing conditions. All mixtures ensured an open print time of at least 40 min. Fresh properties were evaluated by measuring density, flow diameter at 10–15 min and 20–30 min, and yield stress using the slug test (Figure 20). Buildability was assessed by determining the maximum number of printed layers before structural instability (buckling) occurred. The results are summarised in Table 10. The measured yield stress values (determined by applying the slug test) ranged from 1706 Pa to 2408 Pa. The highest yield stress was observed for composition G161 (2408 Pa), while the lowest was observed for G162 (1706 Pa).



(**a**) Buckling test (G162) (**b**) Slug test (G162)

Figure 20. In situ 3DP tests. (**a**) Buckling test. (**b**) Slug test.

Table 10. 3DP mix compositions and fresh mix properties.

Composition No	G159	G160	G161	G162
Fresh density	1927	2010	1975	1982
Slug mass m_s, g (average)	161 ± 3.0	159 ± 1.1	209 ± 6.7	148 ± 4.5
Yield stress, Pa (at 10–15 min)	**1860 ± 35**	**1838 ± 13**	**2408 ± 77**	**1706 ± 52**
Buckling, layers (at 15–20 min)	30.5	39	37	29
Flow diameter at 10–15 min, mm	165	164	174	173
Flow diameter at 20–30 min, mm	155	143	165	167

The buildability results ranged from 29 to 39 layers. The highest number of stable layers was achieved by G160 (39 layers), followed by G161 (37 layers). The lowest buildability was observed for G162 (29 layers). Flow diameter values decreased slightly over time for all mixtures. At 10–15 min, values ranged from 160 mm to 173 mm; at 20–30 min, from 143 mm to 167 mm. Fresh density values ranged from 1927 kg/m^3 to 2010 kg/m^3.

4. Discussion

4.1. Optimisation of GCP Composition

The results indicate that the mechanical and durability performance of GCP systems is governed by the balance between gypsum-driven early hydration and cement–pozzolan reactions at later stages. The insignificant difference between early-age (7-day) and 28-day strength at lower cement contents is associated with a dominant contribution of gypsum hydration, which is consistent with previously reported behaviour of gypsum-based ternary systems [21]. In contrast, mixtures with higher cement and metakaolin contents show significant strength gain over time, reflecting the formation of calcium silicate hydrate

(C–S–H) and the contribution of pozzolanic reactions [42]. Metakaolin plays a critical role in consuming calcium hydroxide and refining the microstructure, contributing to both strength development and durability.

Water resistance behaviour further supports this interpretation. Low cement content results in insufficient formation of water-resistant phases, leading to increased water absorption and a reduced softening coefficient. At the same time, high cement content without adequate pozzolanic addition leads to unbalanced sulfate–aluminate reactions, potentially promoting the formation of expansive phases such as ettringite, which negatively affects durability. The selection of benchmark mixture G10 (55/22.5/22.5) reflects the balance and provides a basis for further evaluation in terms of long-term stability and printability.

4.2. The Effect of Diverse Binder Compounds

4.2.1. Effect of Pozzolan Type on Strength and Durability

Despite a constant binder ratio and similar admixture dosages, significant variations are observed in the softening coefficient (K), water absorption (W), and density reduction ($\Delta\rho$), indicating that pozzolan characteristics govern long-term performance. Three distinct GCP systems can be identified:

High-durability systems ($K \geq 0.75$). Mixtures incorporating metakaolin (MK) (G60–G62), zeolite (G63), and silica fume (G64) exhibit the highest durability performance. These systems are characterised by relatively low water absorption and high softening coefficients. Among these, MK-based mixtures (G60–G62) show the most balanced performance, combining high K values (up to 0.83) with low water absorption and moderate density loss. The composition with SF (G64), while achieving the highest K value (0.87), is associated with significantly higher water absorption (21.3%) and the largest density reduction ($\Delta\rho$ = 284 kg/m^3), suggesting a more complex pore structure despite improved resistance to strength loss.

Moderate-durability systems ($0.60 \leq K < 0.75$). The mixture containing a blend of SF and DM (G71) exhibits intermediate behaviour, with K = 0.63 and elevated water absorption (24.2%). Partial replacement of reactive pozzolan with inert or weakly reactive fillers (DM) appears to reduce overall system stability. This behaviour is consistent with the findings reported by Scrivener et al., who found that dilution of reactive binder phases by inert materials reduces the formation of C–S–H and limits pore refinement, thereby increasing permeability and diminishing durability.

Low-durability systems ($K < 0.60$). Mixtures incorporating DM, OSA, FA, GP, LM, and blended systems (NS + DM) demonstrate significantly reduced durability. These compositions exhibit low softening coefficients (K = 0.39–0.50) and high water absorption (20.9–30.5%). Although calcined clay (LM, G66) is generally considered a reactive pozzolan, its performance in this system (K = 0.40) suggests insufficient reactivity or incompatibility with the gypsum-rich matrix. Likewise, glass powder (G65) and dolomite-based systems (G72, G74) exhibit low durability, indicating that inert or weakly reactive materials do not provide sufficient microstructural refinement. This behaviour is consistent with the findings reported by Scrivener et al., which demonstrate that low-reactivity or inert supplementary materials, as well as poorly activated calcined clays, may not generate sufficient secondary C–S–H/C–A–S–H to densify the microstructure, resulting in higher porosity, increased water absorption, and reduced durability.

A consistent relationship was observed between durability indicators. Mixtures with a higher softening coefficient ($K \geq 0.75$) generally exhibit lower water absorption and smaller density reduction, while low-K mixtures show the opposite trend. The results confirm that highly reactive and fine pozzolans (e.g., MK, SF) provide the most favourable performance in GCP systems. In contrast, inert or heterogeneous materials (e.g., DM, OSA, FA) lead to

reduced durability. The selection of pozzolan type is therefore a critical factor in achieving stable, durable GCP composites.

4.2.2. Mechanisms of Long-Term Deformation

Deformation behaviour is governed by the pozzolan's ability to regulate internal reactions. Reactive pozzolans (e.g., MK, SF) stabilise the system, while inert or unbalanced systems (e.g., DM, OSA) allow gradual accumulation of expansive reactions. Therefore, three distinct deformation behaviours can be identified:

- Stable systems with MK, SF, FA and zeolite (G60–G64, G70–G71): characterised by initial strain followed by stabilisation;
- Progressive instability with OSA and LM (G66–G67): continuous strain accumulation leading to failure;
- Delayed instability with glass powder, dolomite, and blended systems (G65, G72-G75): low initial strain followed by accelerated degradation.

The unstable GCP compositions exhibit pronounced localised cracking, indicating non-uniform internal stress development within the material. The observed crack patterns suggest that damage does not evolve uniformly across the specimen. Localised cracking, rather than uniform degradation, is associated with heterogeneous internal expansion processes. Even under consistent external exposure conditions, internal chemical reactions—such as sulfate–aluminate interactions and reactions involving free calcium hydroxide in OSA-based systems—can proceed unevenly due to local differences in composition and microstructure. These observations are consistent with recent studies showing that highly reactive pozzolans (e.g., MK, SF) refine pore structure and stabilise internal reactions, while low-reactivity or heterogeneous systems promote non-uniform expansion, moisture gradients, and localised cracking in cementitious and gypsum-based composites [43].

4.2.3. Frost Resistance and Durability Limitations

Frost resistance is strongly correlated with capillary water absorption. Mixtures with higher porosity and water uptake exhibit increased scaling and mass loss, consistent with general durability principles for cementitious materials. Among the tested mixtures, G95, G102, and G107 exhibited the highest durability, with softening coefficients of 0.79–0.84 and relatively low water absorption, indicating a dense microstructure and limited moisture ingress. In contrast, mixtures such as G109 and G118-3DP showed significantly lower softening coefficients ($\approx$0.41–0.43), which can be associated with higher capillary water uptake and increased saturation levels before freeze–thaw exposure. Capillary water absorption plays a critical role, as it governs the rate and extent of water penetration into the pore system. Observations are supported by recent studies demonstrating that freeze–thaw resistance is governed by capillary porosity and water absorption, where higher saturation levels lead to increased scaling and mass loss, while dense microstructures formed by reactive pozzolans (e.g., MK) reduce moisture ingress but may not fully compensate for system limitations.

The partial improvement observed with MK addition indicates that pozzolanic stabilisation can mitigate, but not fully eliminate, durability limitations associated with reactive or calcium-rich additives. The degradation observed in the 3D-printed sample (G118-3DP) underscores the importance of long-term durability alongside printability. While certain compositions may be suitable for extrusion, their long-term performance under moisture exposure remains a critical constraint. This finding aligns with recent studies on 3DCP, which emphasise that printability criteria alone are insufficient and must be combined with durability assessment for practical applications. In 3D-printed cementitious mate-

rials, durability is strongly influenced by interlayer porosity and anisotropy, requiring a combined evaluation of printability and long-term performance [44].

4.3. Rheological Characterisation and Printability

The rheological behaviour of GCP mixtures demonstrates pronounced thixotropic characteristics, reflected by decreasing plastic viscosity with increasing shear rate and a progressive increase in yield stress over time. The observed increase in yield stress between 5 and 30 min confirms time-dependent structuration, which is essential for maintaining shape stability in extrusion-based 3D printing. The W/B ratio is identified as a primary controlling parameter governing both flowability and structural build-up. Lower W/B ratios (Mix2) result in higher yield stress and slightly increased plastic viscosity, enhancing shape retention but reducing open print time. Conversely, higher W/B ratios (Mix1) improve workability and extend printability but reduce structural stability. These trends are consistent with established rheological frameworks for printable cementitious materials, where thixotropy and structuration kinetics control buildability and extrusion performance [45].

The incorporation of sand (Mix3) significantly alters rheological behaviour, shifting from thixotropic paste behaviour to friction-dominated flow, as evidenced by a substantial increase in plastic viscosity (up to ~8920 mPa·s). This indicates increased particle interaction and reduced availability of free binder for lubrication, in agreement with observations reported for aggregate-containing systems [46].

Differences between static viscosity (vibration viscometry) and plastic viscosity (rotational rheometry) are attributed to the measurement principles. Vibration viscometry reflects local paste behaviour, while rotational rheometry captures bulk response, including particle interactions and confinement effects. The obtained viscosity values are consistent with previously reported ranges 300–1300 mPa·s for paste systems, although significant variability exists in the literature depending on test methodology.

While good agreement was observed with rheological measurements reported by other authors using similar instruments, significant discrepancies were observed with results from studies conducted on different instruments. The results confirm that rheological behaviour and printability of GCP systems are governed by the interplay between water content, solid fraction, and particle interactions within the composite matrix.

4.4. Rheology–Printability Relationship and In Situ Validation

The relationship between rheological properties and printability indicates that conventional rheometric measurements alone are insufficient to fully characterise material behaviour under real extrusion conditions. Yield stress values obtained from in situ slug tests (>984 Pa) are significantly higher than those determined using rotational rheometry (200–420 Pa), indicating that laboratory-based methods underestimate structural resistance during printing. As highlighted in [47], conventional rheometry does not capture key process-related phenomena such as shear localisation, plug flow, wall slip, and tunnelling effects, all of which contribute to increased apparent resistance during extrusion. In addition, the difficulty in accurately determining static yield stress in highly thixotropic systems further explains the observed divergence between laboratory and in situ measurements.

The obtained yield stress values are consistent with the ranges reported in the literature, although significant variability is observed across methods. For instance, yield stress values ranging from 900 to 3600 Pa have been reported using various techniques [31,48]. In contrast, shear strength values of 500–3000 kPa for high-performance printable concretes were observed in [49], aligning more closely with the in situ slug test results. Similarly, plastic viscosity values show considerable variation across studies. Cement mortars with plastic viscosity up to 2200 mPa·s were reported in, while other studies indicate even higher

values. In the present study, the plastic viscosity values (1500–2500 mPa·s) are comparable to those reported in using similar rheometers, where limited variation over time (5–60 min) was also observed.

The results further demonstrate a direct relationship between yield stress and buildability. Compositions with higher yield stress (e.g., G160, G161) exhibit improved structural stability and sustain a greater number of printed layers before buckling. In contrast, mixtures with lower yield stress (e.g., G162, 1706 Pa) show reduced buildability and earlier structural failure. This confirms that yield stress is a governing parameter controlling load-bearing capacity during layer-by-layer deposition, in agreement with previous findings [44].

Finally, the observed non-linear rheological behaviour indicates that simplified models, such as the Bingham model, may not adequately describe the flow response of GCP mixtures in some cases. Instead, the Herschel–Bulkley model [30,49] which incorporates both yield stress and shear-dependent viscosity, provides a more accurate framework for representing material behaviour:

$$\tau = \tau_0 + K\,\gamma^n. \quad (5)$$

This model is more complex, as it requires the determination of two additional constants (the consistency index K and the flow behaviour index n). Although this model requires additional parameters, it offers improved predictive capability for extrusion-based processes and should be considered in further research. The results demonstrated that reliable prediction of printability requires an integrated approach combining rheological characterisation with in situ validation. Such an approach enables a more accurate assessment of extrusion behaviour and structural performance, supporting the optimisation of GCP mixtures for additive manufacturing applications.

4.5. Limitations and Future Perspectives

Although the present study provides a comprehensive evaluation of mix design, rheological behaviour, and durability of GCP systems for extrusion-based 3D printing, several limitations should be acknowledged. The most significant limitation concerns the incomplete understanding of the mechanisms underlying the expansion and deformation observed during long-term moisture exposure. While experimental results clearly demonstrate progressive expansion and localised cracking in certain compositions, the underlying physicochemical processes—such as delayed ettringite formation, sulfate–aluminate reactions, or interactions involving free calcium hydroxide (particularly in OSA-containing systems)—were not directly characterised in this study. The absence of microstructural (e.g., SEM, XRD) and phase-evolution analyses limits the ability to definitively identify the dominant mechanisms governing volumetric instability. From a practical perspective, this limitation has important implications for the application of GCP systems in 3D printing.

Future research should therefore focus on detailed microstructural and mineralogical investigations, coupled with long-term monitoring, to establish predictive relationships between composition, hydration processes, and dimensional stability. Such studies are essential for ensuring the safe and reliable implementation of GCP-based materials in additive manufacturing.

The characterisation of printability and buildability remains method-dependent and requires further standardisation. In this study, yield stress and viscosity were determined using different approaches (rotational rheometry, vibration viscometry, and extrusion-based tests), which yielded non-equivalent values due to differences in measurement principles, shear conditions, and requirements for mixing consistency. As a result, direct comparison between methods is limited, and the definition of threshold values for printability and buildability remains uncertain. This highlights the need for a unified framework linking

rheological parameters—particularly yield stress and thixotropic structuration—to practical performance indicators such as extrusion stability and layer buildability.

5. Conclusions

Within the scope of this comprehensive study, GCP compositions were specifically developed and characterised for 3D printing, filling an existing research gap in this promising field. By combining the fast-setting properties of gypsum, the durability of Portland cement, and the performance-enhancing properties of pozzolanic materials, this study offers a viable and more sustainable alternative for digital construction.

The optimised GCP mixtures demonstrated high mechanical properties, achieving compressive strengths of up to 40 MPa, a water resistance coefficient of up to 0.85, and water absorption coefficients of no more than 12%, highlighting their potential for construction applications.

Although metakaolin demonstrated consistently high performance, the study showed that not all of the tested pozzolanic components provided sufficient durability. It is important to note that the successful integration of secondary gypsums, such as recycled plasterboard and phosphogypsum, highlights the environmental benefits of this research by promoting the utilisation of industrial by-products and construction waste. The assessment of the sand filler content was also crucial, as it enabled the optimal filler proportion to be determined, providing mechanical strength without compromising 3D printing while significantly reducing the binder proportion.

The optimised GCP composition is a reliable and durable material, as evidenced by laboratory tests. However, when assessing the potential of various industrial by-products and recycled gypsum as pozzolanic components, long-term tests for water and climate resistance are required. The simplest and most reliable test for water resistance is long-term storage of prismatic samples in water, with monitoring of expansion deformation and assessment of crack formation.

The negative effect on durability could be caused by the use of microadditives with a low pozzolanic effect that also contain additional calcium hydroxide.

The most acceptable and durable GCP formulations from the point of view of mechanical strength and durability are a composition with reactive metakaolin and building gypsum, as well as a combination of building gypsum with secondary gypsum (recycled gypsum and phosphogypsum). In addition, the samples demonstrated frost resistance comparable to the performance levels typically associated with XF1 exposure conditions (based on scaling limits).

Rheological studies showed that within 30 min, the yield shear stress of the GCP mixture increased significantly, but the plastic viscosity remained approximately the same. Moreover, the GCP binder pastes exhibited significant thixotropy. In turn, the GCP mixture with sand had a significantly higher viscosity.

Adapting GCP mixtures for 3D printing involves careful adjustment of setting time and rheological properties. The water-to-binder ratio was selected in the range of 0.38–0.45 to ensure the mixture's required buildability, with an open time of 20–40 min. Methods such as the cone flow test, slugs test, and buildability test were used to evaluate the fresh properties.

The results demonstrate that yield stress is the governing rheological parameter for the buildability of GCP mixtures. An increase in yield stress over time reflects structural build-up. This is confirmed by the correlation between higher yield stress values (e.g., G160, G161) and an increased number of stable printed layers.

The results demonstrate the potential to produce a ternary binder-based system with CO_2-reduction potential for low-carbon, 3D-printed GCP elements in low-loaded structures, paving the way for more sustainable construction methods.

Author Contributions: Conceptualisation, G.S. and G.B.; methodology, G.S. and M.S.; software, P.S.; validation, M.S. and A.S.; formal analysis, V.L.; investigation, G.S.; resources, D.B.; data curation, G.S.; writing—original draft preparation, G.S.; writing—review and editing, V.L., G.B. and M.S.; visualisation, P.S. and G.S.; supervision, D.B.; project administration, G.S.; funding acquisition, G.S. All authors have read and agreed to the published version of the manuscript.

Funding: This research is funded by the FLPP (Fundamental and Applied Research Projects) program in Latvia under the research project lzp-2022/1-0585 "Development and characterisation of sustainable gypsum-cement-pozzolanic ternary compositions for 3D printing".

Data Availability Statement: The raw data supporting the conclusions of this article will be made available by the authors on request.

Conflicts of Interest: The authors declare no conflicts of interest.

References

1. UN Environment Programme. *Building Materials and the Climate: Constructing A New Future*; UNEP—UN Environment Programme: Nairobi, Kenya, 2023.
2. Tay, Y.W.D.; Li, M.Y.; Tan, M.J. Effect of Printing Parameters in 3D Concrete Printing: Printing Region and Support Structures. *J. Mater. Process. Technol.* **2019**, *271*, 261–270. [CrossRef]
3. Sinka, M.; Zorica, J.; Bajare, D.; Sahmenko, G.; Korjakins, A. Fast Setting Binders for Application in 3D Printing of Bio-Based Building Materials. *Sustainability* **2020**, *12*, 8838. [CrossRef]
4. Alhumayani, H.; Gomaa, M.; Soebarto, V.; Jabi, W. Environmental Assessment of Large-Scale 3D Printing in Construction: A Comparative Study between Cob and Concrete. *J. Clean. Prod.* **2020**, *270*, 122463. [CrossRef]
5. Mukhametrakhimov, R.; Galautdinov, A.; Lukmanova, L. Influence of Active Mineral Additives on the Basic Properties of the Gypsum Cementpozzolan Binder for the Manufacture of Building Products. *MATEC Web Conf.* **2017**, *106*, 03012. [CrossRef]
6. Stav, E.; Burkard, E.A.; Finkelstein, R.S.; Winkowski, D.A.; Metz, L.J.; Mudd, P.J. Cementitious Gypsum-Containing Binders and Compositions. U.S. Patent US5858083, 12 January 1999.
7. Mukhametrakhimov, R.K.; Galautdinov, A.R.; Gilmanshin, I.R. Modified Gypsum-Cement-Pozzolanic Composites Reinforced with Polypropylene Fibers Modified Gypsum-Cement-Pozzolanic Composites Reinforced with Polypropylene Fibers. *IOP Conf. Ser. Mater. Sci. Eng.* **2019**, *570*, 012068. [CrossRef]
8. Çolak, A. Physical, Mechanical, and Durability Properties of Gypsum—Portland Cement—Natural Pozzolan Blends. *Can. J. Civ. Eng.* **2001**, *28*, 375–382. [CrossRef]
9. Abdellatief, M.; Elemam, W.E.; Alanazi, H.; Tahwia, A.M. Production and Optimization of Sustainable Cement Brick Incorporating Clay Brick Wastes Using Response Surface Method. *Ceram. Int.* **2023**, *49*, 9395–9411. [CrossRef]
10. Fayomi, G.U.; Mini, S.E.; Fayomi, O.S.I.; Ayoola, A.A. Perspectives on Environmental CO_2 Emission and Energy Factor in Cement Industry. *IOP Conf. Ser. Earth Environ. Sci.* **2019**, *331*, 012035. [CrossRef]
11. Bumanis, G.; Korjakins, A.; Bajare, D. Environmental Benefit of Alternative Binders in Construction Industry: Life Cycle Assessment. *Environments* **2022**, *9*, 6. [CrossRef]
12. Zhang, Y.; Pan, F.; Wu, R. Study on the Performance of FGD Gypsum-Metakaolin-Cement Composite Cementitious System. *Constr. Build. Mater.* **2016**, *128*, 1–11. [CrossRef]
13. Bumanis, G.; Vaičiukynienė, D.; Tambovceva, T.; Puzule, L.; Sinka, M.; Nizevičienė, D.; Fornés, I.V.; Bajare, D. Circular Economy in Practice: A Literature Review and Case Study of Phosphogypsum Use in Cement. *Recycling* **2024**, *9*, 63. [CrossRef]
14. Sahmenko, G.; Puzule, L.; Sapata, A.; Slosbergs, P.; Bumanis, G.; Sinka, M.; Bajare, D. Gypsum–Cement–Pozzolan Composites for 3D Printing: Properties and Life Cycle Assessment. *J. Compos. Sci.* **2024**, *8*, 212. [CrossRef]
15. Tseng, K.-C.; Chi, M.; Yeih, W.; Huang, R. Influence of Slag/Fly Ash as Partial Cement Replacement on Printability and Mechanical Properties of 3D-Printed Concrete. *Appl. Sci.* **2025**, *15*, 3933. [CrossRef]
16. Girskas, G.; Kligys, M. 3D Concrete Printing Review: Equipment, Materials, Mix Design, and Properties. *Buildings* **2025**, *15*, 2049. [CrossRef]
17. Doleželová, M.; Pokorný, J.; Vimmrová, A. Design of the Ternary Gypsum-Based Building Composite Using Simplex Optimization. In *Materials Design and Applications II*; Springer Nature: Cham, Switzerland, 2018. [CrossRef]

18. Ma, G.; Buswell, R.; Leal da Silva, W.R.; Wang, L.; Xu, J.; Jones, S.Z. Technology Readiness: A Global Snapshot of 3D Concrete Printing and the Frontiers for Development. *Cem. Concr. Res.* **2022**, *156*, 106774. [CrossRef]
19. Bumanis, G.; Zorica, J.; Bajare, D. Properties of Foamed Lightweight High-Performance Phosphogypsum-Based Ternary System Binder. *Appl. Sci.* **2020**, *10*, 6222. [CrossRef]
20. Colak, A. The Long-Term Durability Performance of Gypsum—Portland Cement—Natural Pozzolan Blends. *Cem. Concr. Res.* **2002**, *32*, 109–115. [CrossRef]
21. Gaidučis, S.; Žvironaitė, J.; Mačiulaitis, R.; Jakovlev, G. Resistance of Phosphogypsum Cement Pozzolanic Compositions against the Influence of Water. *Mater. Sci.* **2011**, *17*, 308–313. [CrossRef]
22. Cengiz, O. Effects of Pozzolan Incorporation and Curing Conditions on Strength and Water Resistance of Natural Gypsum Pastes. Ph.D. Thesis, Middle East Technical University, Ankara, Turkiye, 2009.
23. da Cruz, T.A.M.; Geraldo, R.H.; Costa, A.R.D.; Maciel, K.R.D.; Goncalves, J.P.; Camarini, G. Microstructural and Mineralogical Compositions of Metakaolin-Lime-Recycled Gypsum Plaster Ternary Systems. *J. Build. Eng.* **2022**, *47*, 103770. [CrossRef]
24. Tayibi, H.; Choura, M.; López, F.A.; Alguacil, F.J.; López-Delgado, A. Environmental Impact and Management of Phosphogypsum. *J. Environ. Manag.* **2009**, *90*, 2377–2386. [CrossRef]
25. Bumanis, G.; Bajare, D.; Korjakins, A. Durability of High Strength Self Compacting Concrete with Metakaolin Containing Waste. *Key Eng. Mater.* **2016**, *674*, 65–70. [CrossRef]
26. Hanžič, L.; Štefančič, M.; Šter, K.; Serjun, V.Z.; Šinka, M.; Sapata, A.; Šahmenko, G.; Šerelis, E.; Migliniece, B.; Bensa, L.K. Collision Milling of Oil Shale Ash as Constituent Pretreatment in Concrete 3D Printing. *Infrastructures* **2025**, *10*, 18. [CrossRef]
27. *EN 196-3:2016*; Cement Testing Methods for Setting Times and Soundness. iTeh Inc.: Newark, DE, USA, 2016. Available online: https://standards.iteh.ai/catalog/standards/cen/e4921eca-8101-4261-b066-25d19b9b8e8a/en-196-3-2016 (accessed on 23 February 2026).
28. *EN 1015-3:1999*; Test Methods for Fresh Mortar Consistence by Flow Table. iTeh Inc.: Newark, DE, USA, 2016. Available online: https://standards.iteh.ai/catalog/standards/cen/f427f20a-2746-4ab7-bd55-d1c455b1f009/en-1015-3-1999 (accessed on 23 February 2026).
29. Jo, J.H.; Jo, B.W.; Cho, W.; Kim, J.-H. Development of a 3D Printer for Concrete Structures: Laboratory Testing of Cementitious Materials. *Int. J. Concr. Struct. Mater.* **2020**, *14*, 13. [CrossRef]
30. Rehman, A.U.; Kim, J.-H. 3D Concrete Printing: A Systematic Review of Rheology, Mix Designs, Mechanical, Microstructural, and Durability Characteristics. *Materials* **2021**, *14*, 3800. [CrossRef]
31. Kligys, M.; Girskas, G.; Baltuškienė, D. Influence of the Amount of Mineral Additive on the Rheological Properties and the Carbon Footprint of 3D-Printed Concrete Mixtures. *Buildings* **2026**, *16*, 490. [CrossRef]
32. Mechtcherine, V.; Muthukrishnan, S.; Robens-Radermacher, A.; Wolfs, R.; Versteege, J.; Menna, C.; Ozturk, O.; Ozyurt, N.; Roupec, J.; Richter, C.; et al. Mechanical Properties of 3D Printed Concrete: A RILEM 304-ADC Interlaboratory Study–Compressive Strength and Modulus of Elasticity. *Mater. Struct./Mater. Constr.* **2025**, *58*, 181. [CrossRef]
33. *EN 196-1:2016*; Cement Strength Testing Methods Compressive Flexural. iTeh Inc.: Newark, DE, USA, 2016. Available online: https://standards.iteh.ai/catalog/standards/cen/37b8816e-4085-4dcc-a642-a383d9bddd6c/en-196-1-2016?srsltid=AfmBOoo6fTjBXuSVef0COQsDcldKbI19Cvg3dzeaEfyZAuHY1ml7m_1l (accessed on 19 April 2026).
34. *EN 1015-18:2002*; Mortar Water Absorption Coefficient Test Method. iTeh Inc.: Newark, DE, USA, 2002. Available online: https://standards.iteh.ai/catalog/standards/cen/d9e520b3-5f88-4368-ae91-e568d18aef5a/en-1015-18-2002?srsltid=AfmBOopEGmoqCc9DwZ0gCXZ9N_I1hWv31ZnVnFtvUVsnjfitJMZFANce (accessed on 19 April 2026).
35. *CEN/TS 12390-9:2016*; Concrete Freeze-Thaw Resistance with De-Icing. iTeh Inc.: Newark, DE, USA, 2016. Available online: https://standards.iteh.ai/catalog/standards/cen/ba399d8b-cdd7-419d-87f0-c00b3033fcd9/cen-ts-12390-9-2016?srsltid=AfmBOopzWpPQW70_a3sMhNs47yV_eCn1gMQsElsW5DqFEUp845cKj7vY (accessed on 19 April 2026).
36. *BS EN 206:2013+A1:2016*; Concrete. Specification, Performance, Production and Conformity-European Standards. iTeh Inc.: Newark, DE, USA, 2016. Available online: https://standards.iteh.ai/catalog/standards/cen/b22aa5df-b7d0-4073-a729-d8e0653c4c49/en-206-2013a1-2016?srsltid=AfmBOopcQtv1ffUDD0auA07EcezdjQFqShrCngzR0FC3zqIMugSDtAUH (accessed on 31 July 2020).
37. *EN 772-11:2011*; Test Methods for Water Absorption of Masonry Units. iTeh Inc.: Newark, DE, USA, 2016. Available online: https://standards.iteh.ai/catalog/standards/cen/ef19ac4d-a314-4036-9e64-fe9db764adba/en-772-11-2011?srsltid=AfmBOopxj-MeOgGGJyLz-_C7d_Nw0U-UhvCC-2rxr0zWraqd1DN9BFGk (accessed on 19 April 2026).
38. Puzule, L.; Spurina, E.; Frolovs, G.; Dragons, D.; Dias, A.C.; Sinka, M. 3D Printing of Bio-Based Building Materials—Mix Design, Properties and Carbon Footprint Assessment. Available online: https://papers.ssrn.com/sol3/papers.cfm?abstract_id=6478099 (accessed on 19 April 2026).
39. Sapata, A.; Šinka, M.; Šahmenko, G.; Korat Bensa, L.; Hanžič, L.; Šter, K.; Ručevskis, S.; Bajāre, D.; Bos, F.P. Establishing Benchmark Properties for 3D-Printed Concrete: A Study of Printability, Strength, and Durability. *J. Compos. Sci.* **2025**, *9*, 74. [CrossRef]

40. OriginLab Help Online-Tutorials-Ternary Contour. Available online: https://www.originlab.com/doc/Tutorials/TernaryContour (accessed on 19 April 2026).
41. Piotrowski, T. Special Requirements for Freeze-Thaw Resistance of Concrete in PWR Nuclear Civil Works. *Mater. Bud.* **2016**, *1*, 95–98. [CrossRef]
42. Wild, S.; Khatib, J.M.; Jones, A. Relative Strength, Pozzolanic Activity and Cement Hydration in Superplasticised Metakaolin Concrete. *Cem. Concr. Res.* **1996**, *26*, 1537–1544. [CrossRef]
43. Sun, D.; Wu, K.; Shi, H.; Miramini, S.; Zhang, L. Deformation Behaviour of Concrete Materials under the Sulfate Attack. *Constr. Build. Mater.* **2019**, *210*, 232–241. [CrossRef]
44. Liu, H.; Liu, C.; Wu, Y.; Bai, G.; He, C.; Zhang, R.; Wang, Y. Hardened Properties of 3D Printed Concrete with Recycled Coarse Aggregate. *Cem. Concr. Res.* **2022**, *159*, 106868. [CrossRef]
45. Roussel, N. Rheological Requirements for Printable Concretes. *Cem. Concr. Res.* **2018**, *112*, 76–85. [CrossRef]
46. Wang, C.; Lian, J.; Fang, Y.; Fan, G.; Yang, Y.; Huang, W.; Shi, S. Rheological Optimization of 3D-Printed Cementitious Materials Using Response Surface Methodology. *Materials* **2025**, *18*, 3933. [CrossRef] [PubMed]
47. Jayathilakage, R.; Rajeev, P.; Sanjayan, J. Rheometry for Concrete 3D Printing: A Review and an Experimental Comparison. *Buildings* **2022**, *12*, 1190. [CrossRef]
48. Le, T.T.; Austin, S.A.; Lim, S.; Buswell, R.A.; Gibb, A.G.F.; Thorpe, T. Mix Design and Fresh Properties for High-Performance Printing Concrete. *Mater. Struct.* **2012**, *45*, 1221–1232. [CrossRef]
49. Si, W.; Khan, M.; McNally, C. A Comprehensive Review of Rheological Dynamics and Process Parameters in 3D Concrete Printing. *J. Compos. Sci.* **2025**, *9*, 299. [CrossRef]

Disclaimer/Publisher's Note: The statements, opinions and data contained in all publications are solely those of the individual author(s) and contributor(s) and not of MDPI and/or the editor(s). MDPI and/or the editor(s) disclaim responsibility for any injury to people or property resulting from any ideas, methods, instructions or products referred to in the content.